**Diese Arbeit wurde vorgelegt am**
**Lehrstuhl für Mathematik (MathCCES)**

# Modellierung und Simulation von Offshore Windparks

## Modeling and simulation of offshore wind farms

Bachelorarbeit
Computational Engineering Science

September 2015

| | |
|---|---|
| Vorgelegt von<br>Presented by | Gregor Heiming<br>Johanniterstr. 30, 52064 Aachen<br>Matrikelnummer: 310620<br>gregor.heiming@rwth-aachen.de |
| Erstprüfer<br>First examiner | Prof. Dr. Martin Frank<br>Lehrstuhl für Mathematik (MathCCES)<br>RWTH Aachen University |
| Zweitprüfer<br>Second examiner | Prof. Dr. Erika Ábrahám<br>Lehr- und Forschungsgebiet Theorie der hybriden Systeme<br>RWTH Aachen University |
| Koreferent<br>Co-supervisor | Dipl.-Math. Dipl.-Inform. Pascal Richter<br>Lehrstuhl für Mathematik (MathCCES)<br>RWTH Aachen University |

# Contents

**Nomenclature** V

**Acronyms** VI

**List of Figures** VII

**List of Tables** VIII

**1 Introduction** 1

**2 State of the art** 2
2.1 Wake models . . . 2
2.2 Cost models . . . 3
2.3 Optimization approaches . . . 3

**3 Model** 5
3.1 Turbine properties . . . 5
3.2 Wind data . . . 6
3.2.1 A Maximum likelihood estimate for the Weibull parameters . . . 7
3.2.2 Quality of the Weibull fit for representing wind data . . . 11
3.3 Annual energy production . . . 14
3.4 PARK wake model . . . 15
3.5 Modified PARK wake model . . . 17
3.6 Eddy-Viscosity wake model . . . 18
3.6.1 Eddy viscosity turbulence closure . . . 19
3.6.2 Discretization . . . 21
3.6.3 Boundary conditions . . . 24
3.6.4 Solution . . . 25
3.6.5 Wake generated turbulence . . . 26
3.6.6 Wake rotor intersections . . . 27
3.7 Cost Model . . . 29

**4 Software** 30
4.1 Implementation . . . 30
4.2 Openwind . . . 31
4.2.1 Input files . . . 31

**5 Verification and results** 32
5.1 Verification of the AEP computation . . . 32
5.1.1 One turbine, constant power curve, one wind direction . . . 32
5.1.2 One turbine, constant power curve, wind data of one year . . . 33
5.1.3 One turbine, real power curve . . . 33

5.2 Verification of the wake models . . . . . 35
5.2.1 Analytical reference value for PARK/Modified PARK . . . . . 35
5.2.2 Verification of the wake rotor intersection in the Eddy-Viscosity model . . . . . 35
5.2.3 Fully shaded turbine . . . . . 36
5.2.4 Partially shaded turbine with PARK . . . . . 37
5.2.5 Intersecting wakes . . . . . 37
5.2.6 Ten turbines in a row . . . . . 37
5.2.7 Development of the centerline velocity deficit . . . . . 39
5.3 Validation of discretization schemes for the Eddy-Viscosity model . . . 40
5.4 Optimization of the Horns Rev 1 offshore wind farm . . . . . 43

**6 Conclusion & Outlook** **47**

**References** **48**

# Nomenclature

### Symbols

| | | |
|---|---|---|
| $\beta_k$ | Shadowing factor | |
| $C_t$ | Thrust coefficient | |
| $D$ | Diameter of the turbine rotor | [m] |
| $\delta u$ | Velocity deficit | |
| $\varepsilon$ | Eddy viscosity | [$m^2/s$] |
| $I_a$ | Ambient turbulence intensity | |
| $I_{tot}$ | Total turbulence intensity | |
| $I_w$ | Wake-induced turbulence intensity | |
| $\kappa$ | Von Kármán constant | |
| $k$ | Wake decay constant | |
| $K_M$ | Eddy diffusivity | [$m^2/s$] |
| $r$ | Radial distance, radius | [m] |
| $\rho$ | Air density | [$kg/m^3$] |
| $u$ | Velocity in downstream direction | [m/s] |
| $u_0$ | Free stream velocity | [m/s] |
| $v$ | Velocity in radial direction | [m/s] |
| $x$ | Downstream distance | [m] |
| $z$ | Hub height of turbine | [m] |
| $z_0$ | Surface roughness of the site | [m] |

### Subscripts

| | |
|---|---|
| 0 | Undisturbed, concerning the site |
| $a$ | Ambient |
| $c$ | Centerline |
| $inc$ | Incident |
| $n$ | Near wake |
| $r$ | Directly behind rotor |
| $w$ | Wake |

# Acronyms

| | |
|---|---|
| **AEP** | Annual energy production |
| **CDF** | Cumulative distribution function |
| **EV** | Eddy-Viscosity |
| **GA** | Genetic algorithm |
| **GIS** | Geographic information system |
| **HAWT** | Horizontal-axis wind turbine |
| **LCOE** | Levelized cost of energy |
| **NS** | Navier-Stokes |
| **ODE** | Ordinary differential equation |
| **PDE** | Partial differential equation |
| **PDF** | Probability density function |
| **RANS** | Reynolds-averaged Navier-Stokes |
| **RMSE** | Root-mean-squared error |
| **RNA** | Rotor nacelle assembly |
| **WFLOP** | Wind farm layout optimization problem |

# List of Figures


1 Turbine measurements . . . . . 5
2 Characteristic curves of wind turbine Enercon E-82 . . . . . 6
3 Wind direction distribution at FINO3 for the years 2011 to 2014 . . . . 9
4 Wind speed distributions at FINO3 for the years 2011 to 2014 . . . . . 10
5 Comparison of annual wind speed distributions . . . . . 11
6 Comparison of distribution fits with clustered measured data . . . . . 13
7 Root-mean-squared errors for distribution fits . . . . . 13
8 Visualization of the wake as described in PARK . . . . . 15
9 Calculation of the shadowing factor $\beta_k$ in original an modified PARK . 18
10 Comparison of radial speed distributions with different filter functions . 20
11 Filter function $F(x)$ for the eddy viscosity in the near-wake . . . . . 21
12 Wake turbine intersections in Eddy-Viscosity . . . . . 28
13 Class diagram . . . . . 30
14 AEP verification: One turbine with a constant power curve and one wind direction . . . . . 32
15 AEP verification: One turbine with a constant power curve . . . . . 33
16 AEP verification: One turbine and one wind direction . . . . . 34
17 AEP verification: One turbine and 12 wind directions . . . . . 34
18 Test setup: Partially shaded turbine . . . . . 37
19 Test setup: Intersecting wakes . . . . . 38
20 Test setup: Ten turbines in a row . . . . . 38
21 Development of the centerline velocity deficit . . . . . 40
22 Analysis of the discretization grid size. Backward Euler . . . . . 41
23 Analysis of the discretization grid size. Crank-Nicolson . . . . . 42
24 Layout of the Horns Rev offshore wind farm . . . . . 43
25 Convergence of a free optimization of Horns Rev . . . . . 44
26 Freely optimized positions for the Horns Rev wind farm . . . . . 45
27 Convergence of the optimization of Horns Rev on a regular grid . . . . 45
28 Optimized positions for the Horns Rev wind farm on a grid structure . 46

# List of Tables


1 Costs respected in OWFLO and TopFarm . . . . . 3
2 Quality of fitted distributions to measured wind data . . . . . 12
3 Openwind simulation parameters used for wake model verification . . . 35
4 Parameters for testing wake models with two turbines in a row . . . . . 36
5 Test results: Two turbines in a row . . . . . 38
6 Test results: Partially shaded turbine . . . . . 38
7 Test results: Intersecting wakes . . . . . 39
8 Test results: Ten turbines in a row . . . . . 39
9 Simulation parameters for the optimization of Horns Rev . . . . . 43

# 1 Introduction

Wind is one of the leading forms of renewable energy production as it is always present compared to solar energy, which can only be efficiently used in certain parts of the world and not during the night. The kinetic energy of the wind is transferred into electrical energy using wind turbines.

For cost reduction reasons, the wind turbines are clustered to wind farms. This makes the installation, maintenance and grid connection easier and cheaper. On the other hand, the clustering of wind turbines leads to energy reduction due to turbulence and undirected flow behind the turbines.

It is desirable to choose the positioning of the wind turbines such that the impact of wake effects is minimized, i.e. the wind farm energy output is maximized. This problem is known as the wind farm layout optimization problem (WFLOP).

As it is computationally expensive to numerically solve the equations describing the turbulent flow, there are simplified models approximating the speed of the directed, exploitable flow. Two of such models (and a modification for one of them) are presented in this thesis. With a computationally cheap wake computation it is possible to solve the WFLOP with different optimization approaches.

Wind farms are divided into onshore and offshore wind farms. The reasons for building offshore wind farms, which are difficult to access compared to onshore wind farms (as there is no existing infrastructure), are the following: The wind offshore is often stronger than onshore and the flow field is more homogeneous as there are no hills, trees or buildings disturbing the flow. Furthermore the noise occurring at the turbine blade tips does not bother at sea. In this thesis, only the offshore case is considered as it covers the basic modeling of wind farms. The simulation of onshore wind farms can be implemented in the future as an extension of the here described models.

This thesis gives an insight into the wake modeling, the simulation of wind farms and the solution of the WFLOP. In section 2 an overview of the literature on modeling and optimization of wind farms is given. Section 3 consists of the model descriptions: The calculation of the annual energy production (AEP), the treatment and representation of wind data, and the wake models PARK, modified PARK and Eddy-Viscosity. Finally a simple cost function is presented. The implementation of the models is briefly described in section 4. In section 5 the models are validated using test cases before they are applied in the optimization of the offshore wind farm Horns Rev in subsection 5.4. In the last section 6 a proposal for the future work on this project is given.

# 2 State of the art

The modeling of offshore wind farms is a subject in literature since the early 1980s. Publications on wind farms can be partitioned into three major categories: The modeling of wake effects, which are responsible for energy reductions in wind farms, the development of cost functions and the optimization of the wind farm layout. In [34] and [36] the state of the art of wake models, cost models and optimization approaches for the WFLOP are summarized. Comparisons and evaluations of several models were published by Barthelmie et al. [3] and Beaucage et al. [4].

## 2.1 Wake models

The first notable wake model was developed and published by Jensen [19] in 1983 and Katic et al. [21] in 1986. This model was used in the computer program PARK [20] as a simple and fast model, that can be used for optimizing wind farm layouts. The PARK model is designed for far wake cases, i.e. it can be used for calculations at a downstream distance of at least three rotor diameters ($3D$) [4]. Although the velocity deficit calculated by the model has a top-hat shape, the computations are quite accurate [3]. For further descriptions of PARK, see section 3.4.

Another remarkable model is the one published by Ainslie [1] in 1988. It is based on a numerical solution of the thin-shear layer approximation of the Navier-Stokes (NS) equations in cylindrical coordinates with several assumptions, e.g. axial symmetry and an eddy viscosity turbulence closure [3]. The model is therefore referred to as Eddy-Viscosity (EV) wake model in the following. It is valid for downstream distances of two rotor diameters ($2D$) or more [4]. Lange et al. [23] developed an extension for the Eddy-Viscosity model, which improves the results of the wake simulations in offshore cases. The EV model is described in detail in section 3.6.

The model developed by Larsen et al. [24] is based on the EV model but its focus is more on the calculation of the wake meandering than on the calculation of the velocity deficit.

Ott [27] introduced a model that is based on the linearized Reynolds-averaged Navier-Stokes (RANS) equations. This leads to good results with a relatively small computational expense.

The developers of Openwind [37] implemented the so-called Deep-array wake model [5]. With this model they try to achieve better results for turbines that are affected by several upwind turbines.

Stovall et al. [35] simulated the atmospheric boundary layer in OpenFOAM using Large Eddy Simulations (LES) and RANS solvers with the intention of giving reference values for the improvement of simple models such as PARK.

Getting even more accurately the wake properties of horizontal-axis wind turbines (HAWTs), Vermeer et al. [38] investigated the wake decay in experiments with controlled flow conditions.

## 2.2 Cost models

In some situations it is not only required to optimize the positions of a fixed number of wind turbines but e.g. the ideal number of turbines in a given area may be desired. In such a case instead of optimizing the expected annual energy output the costs for the wind farm need to be minimized. The therefore used cost function can have a varying scope. There is a simple cost model where the levelized cost of energy (LCOE) only depends on the number of turbines in the wind farm. This model was repeatedly used in wind farm layout optimization [14, 26, 40].

On the other hand there are two more complex cost models that consider more parameters [36]. One is presented by Elkinton et al. [9] and used in the OWFLO project. The other one introduced by Réthoré et al. [32] is implemented in the TopFarm software. The models are based on very different ideas. TopFarm only calculates relative costs, which are costs that depend on the wind farm layout, while OWFLO computes the absolute costs of the wind farm. In table 1 the costs that are respected in these models are listed.

| | **OWFLO** | **TopFarm** |
|---|---|---|
| Foundation | ✓ | ✓ |
| Electrical grid | ✓ | ✓ |
| Maintenance | ✓ | ✓ |
| Degradation | ✓ | ✓ |
| Decommissioning | ✓ | ✓ |
| Rotor nacelle assembly (RNA) | ✓ | |
| Inflation | | ✓ |
| Interest | | ✓ |

Table 1: Costs respected in OWFLO and TopFarm, see [36]

## 2.3 Optimization approaches

There are several approaches for solving the WFLOP in literature. Especially meta-heuristic models are widely spread in the optimization of wind farms, whereof genetic algorithms (GAs) are the most common [36]. Mosetti et al. [26] used a GA to optimize wind farms with a multi-objective function of power and costs on a grid of discrete positions [34]. It is the first work on GAs in wind farm layout optimization and forms the foundation for other works. Grady et al. [14] also used a GA, but modified the parameters to get even better results. Other optimization approaches using GAs can be found in [25] and [40]. In the genetic algorithms mentioned above the solution space is discrete, which distinguishes these from the one used in this thesis [17].

Another meta-heuristic approach was developed by Eroğlu and Seçkiner [10]. They use an ant colony algorithm for optimizing the wind farm layout by maximizing the expected energy output for different wind scenarios.

The method by Wan et al. [41] is based on a particle swarm algorithm. It optimizes turbine placement in the continuous space and considers a fixed minimal distance between turbines.

Ituarte-Villarreal and Espiritu [16] presented a viral based optimization algorithm, which yields good results for simple cases. However the algorithm needs to be developed further for more complex problems, e.g. more than one wind direction and speed.

Pérez et al. [29] published a paper on a two-step optimization for the wind farm layout. For the first step they implemented a heuristic method to set a layout to be optimized. As a second step they optimize locally using nonlinear mathematical programming techniques.

# 3 Model

In this section the different fields of modeling offshore wind farms are examined. The first part is about wake model independent equations and parameters: In subsection 3.1 the turbine properties are described. The following subsection 3.2 deals with the representation of wind speed and direction data and the analysis of measured data. In subsection 3.3 the calculation of the annual energy production (AEP) dependent of the wind distribution is presented. Subsequently the wake models are presented: PARK, modified PARK and Eddy-Viscosity (EV). Finally this is followed by the description of a simple cost function.

## 3.1 Turbine properties

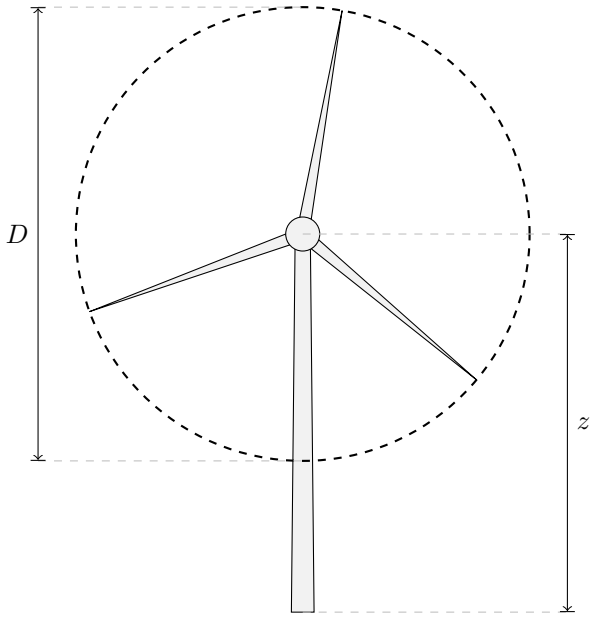


Figure 1: Turbine measurements

There are different types of wind turbines. The most common type is a horizontal-axis wind turbine (HAWT) and consists of 3 blades where the propulsion mainly comes from the lift force perpendicular to the blades. As it is the most common type it is also the only one that is considered in this thesis. HAWTs are characterized by their hub height $z$ and their rotor diameter $D$, see figure 1, a cut-in speed $u_{cutin}$ and a cut-out speed $u_{cutout}$. Cut-in speed and cut-out speed specify the range of wind speed, in which the turbine is working. If the wind speed is lower than $u_{cutin}$ there is not enough wind for efficient power production, and for wind speeds larger than $u_{cutout}$ the turbine may be damaged. Furthermore, wind turbines have a power curve specifying the power output, a thrust curve specifying the thrust coefficient, and an RPM curve specifying the revolutions per minute, all of them depending on the incident wind speed. There

are often several curves for different air density values. However, in this work it is assumed that the density is constant at $1.225\,\mathrm{kg/m^3}$, which is the air density at a temperature of 15 °C at sea level. As an example, figure 2 shows the characteristic curves of the wind turbine E-82 by Enercon. The curves start at 2 m/s and end at 25 m/s as this is the cut-in and respectively the cut-out wind speed of the considered turbine.

The thrust coefficient $C_t$ defined by the turbine's $C_t$ curve influences the thrust that affects the turbine rotor [15]. Therefore it is a measure for the velocity leap at the rotor as well. The velocity deficit is lower for small values of $C_t$ and grows with an increasing thrust coefficient.

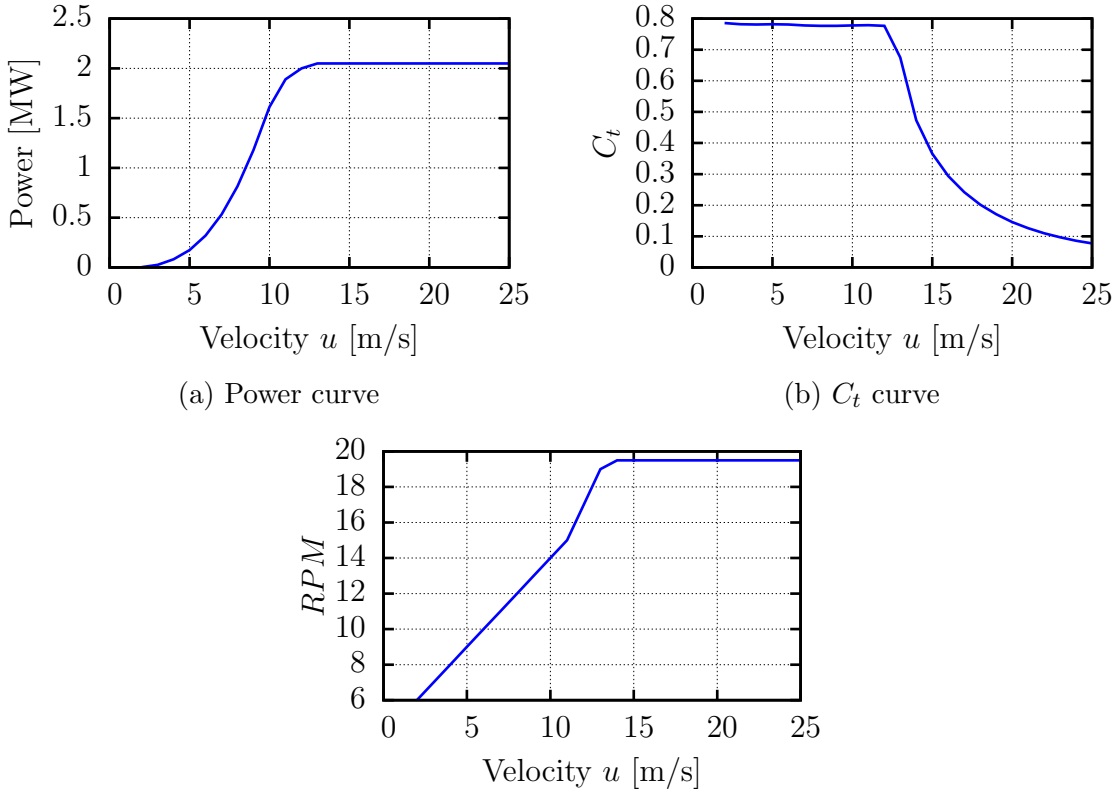


(a) Power curve

(b) $C_t$ curve

(c) RPM curve

Figure 2: Characteristic curves of wind turbine Enercon E-82, from Openwind [37]

## 3.2 Wind data

When using real wind data measured by an anemometer, we first have to process it. The measured data typically consists of thousands of pairs of wind speed and direction. The datasets are then clustered by wind direction, usually in 12 to 72 sectors of equal width (in angle). The probability for the wind blowing from one of the directions is determined by the fraction of datasets in that direction sector.

Instead of also clustering the speed data a speed probability distribution function is set up by fitting it to the measured data for each direction sector. This way, only the parameters describing the distribution are saved instead of a probability value for each speed class. Furthermore, there is no requirement to choose an integration method for the integral in equation (7) at this point.

As the Weibull distribution is a good approximation to measured wind speed data [8], it is used for representing the measured data. The Weibull distribution is described by the scale parameter $A$ and the shape parameter $k$, and its probability density function is defined as follows:

$$f_{A,k}(x) = \left(\frac{k}{A}\right)\left(\frac{x}{A}\right)^{k-1} \exp\left(-\left(\frac{x}{A}\right)^{k}\right). \tag{1}$$

The goodness of the Weibull distribution as an approximation to the measured data is examined in subsection 3.2.2.

### 3.2.1 A Maximum likelihood estimate for the Weibull parameters

For approximating the Weibull density function to the measured values, we have to estimate the two Weibull parameters $A$ and $k$. This will be done using the method of maximum likelihood [11]. Therefore, the natural logarithm of the likelihood function

$$L(A,k;x) = L(A,k;x_0,x_1,...,x_{N-1}) = f_{A,k}(x_0,x_1,...,x_{N-1}) = \prod_{i=0}^{N-1} f_{A,k}(x_i), \tag{2}$$

where $N$ is the number of of speed data, is derived by $A$ and $k$ respectively and both derivations are equated to zero. The resulting equations are then solved for the two parameters $A$ and $k$.

$$\begin{aligned}
\log L(A,k;x) &= \log \prod_{i=0}^{N-1} f_{A,k}(x_i) \\
&= \log \prod_{i=0}^{N-1} \left(\frac{k}{A}\right)\left(\frac{x_i}{A}\right)^{k-1} \exp\left(-\left(\frac{x_i}{A}\right)^{k}\right) \\
&= \sum_{i=0}^{N-1} \log\left(\left(\frac{k}{A}\right)\left(\frac{x_i}{A}\right)^{k-1} \exp\left(-\left(\frac{x_i}{A}\right)^{k}\right)\right) \\
&= \sum_{i=0}^{N-1} \log(k) - k\log(A) + (k-1)\log(x_i) - \left(\frac{x_i}{A}\right)^{k} \\
&= N\log(k) - Nk\log(A) + (k-1)\sum_{i=0}^{N-1}\log(x_i) - A^{-k}\sum_{i=0}^{N-1} x_i^k
\end{aligned} \tag{3}$$

The likelihood function is now derived by $A$

$$\frac{\partial}{\partial A}\log L(A,k;x) = -\frac{Nk}{A} + kA^{-(k+1)}\sum_{i=0}^{N-1} x_i^k = 0$$

$$\Leftrightarrow NA^k = \sum_{i=0}^{N-1} x_i^k$$

$$\Leftrightarrow A = \left( \frac{1}{N} \sum_{i=0}^{N-1} x_i^k \right)^{1/k} \tag{4}$$

and by $k$:

$$\frac{\partial}{\partial k} \log L(A, k; x) = \frac{N}{k} - N \log(A) + \sum_{i=0}^{N-1} \log(x_i) - \sum_{i=0}^{N-1} \left( \frac{x_i}{A} \right)^k \log \left( \frac{x_i}{A} \right) = 0$$

$$\begin{aligned}
\Leftrightarrow \quad & \frac{1}{k} - \log(A) + \frac{1}{N} \sum_{i=0}^{N-1} \log(x_i) \\
& - \frac{1}{N} \left[ \frac{1}{A^k} \sum_{i=0}^{N-1} x_i^k \log(x_i) - \frac{1}{A^k} \sum_{i=0}^{N-1} x_i^k \log(A) \right] = 0 \\
\Leftrightarrow \quad & \frac{1}{k} - \log \left( \left( \frac{1}{N} \sum_{i=0}^{N-1} x_i^k \right)^{1/k} \right) + \frac{1}{N} \sum_{i=0}^{N-1} \log(x_i) \\
& - \frac{1}{N} \left[ \left( \left( \frac{1}{N} \sum_{i=0}^{N-1} x_i^k \right)^{1/k} \right)^{-k} \sum_{i=0}^{N-1} x_i^k \log(x_i) \right. \\
& \left. - \left( \left( \frac{1}{N} \sum_{i=0}^{N-1} x_i^k \right)^{1/k} \right)^{-k} \sum_{i=0}^{N-1} x_i^k \log \left( \left( \frac{1}{N} \sum_{i=0}^{N-1} x_i^k \right)^{1/k} \right) \right] = 0 \\
\Leftrightarrow \quad & \frac{1}{k} - \frac{1}{k} \log \left( \frac{1}{N} \sum_{i=0}^{N-1} x_i^k \right) + \frac{1}{N} \sum_{i=0}^{N-1} \log(x_i) \\
& - \frac{\sum_{i=0}^{N-1} x_i^k \log(x_i)}{\sum_{i=0}^{N-1} x_i^k} + \frac{\sum_{i=0}^{N-1} x_i^k \frac{1}{k} \log \left( \frac{1}{N} \sum_{i=0}^{N-1} x_i^k \right)}{\sum_{i=0}^{N-1} x_i^k} = 0 \\
\Leftrightarrow \quad & \frac{1}{k} + \frac{1}{N} \sum_{i=0}^{N-1} \log(x_i) - \frac{\sum_{i=0}^{N-1} x_i^k \log(x_i)}{\sum_{i=0}^{N-1} x_i^k} = 0
\end{aligned} \tag{5}$$

As equation (5) can't be solved analytically we use the Newton-Raphson method to get the shape parameter $k$. The scale parameter $A$ can then be found by placing $k$ in equation (4).

The following figures show the wind direction and speed distributions of the years

2011 to 2014 measured at the FINO3 research platform[1], which is located in the German North Sea. In figure 3 the probabilities for the direction sectors are visualized for data clustered into 12 direction sectors. Figure 4 shows the fitted direction-independent Weibull probability density functions (PDFs) for the years 2011 to 2014 respectively. This corresponds to a single direction sector of 360°. In figure 5 the fitted distributions of the four years are compared to their mean. From the differences between the fitted Weibull density functions in figure 5 it can be seen that the wind distributions slightly change from year to year. The annual energy production calculated by the simulation depends on the wind data used. To be able to make meaningful predictions for the energy output of a wind farm one either has to find a typical year or use measured data from several years.

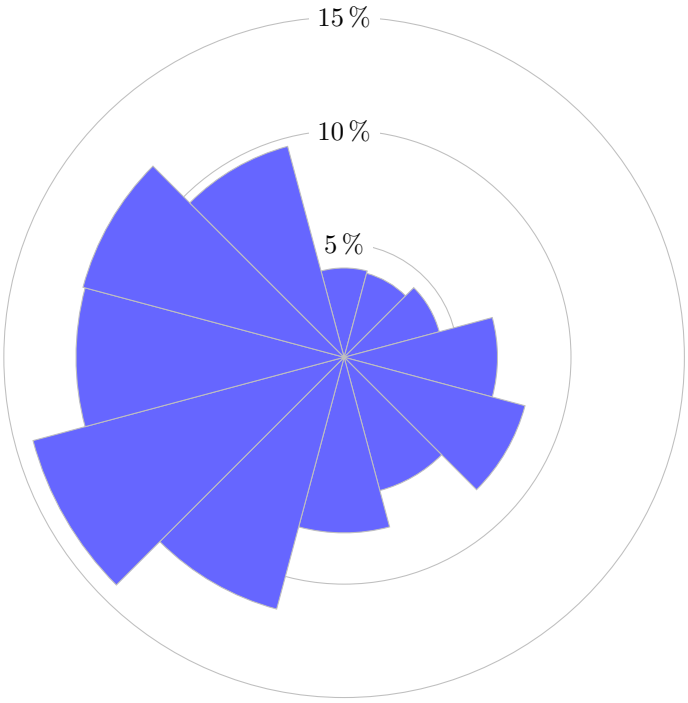


Figure 3: Combined wind direction distribution at FINO3 for the years 2011 to 2014, clustered into 12 direction sectors

[1] http://www.fino3.de/

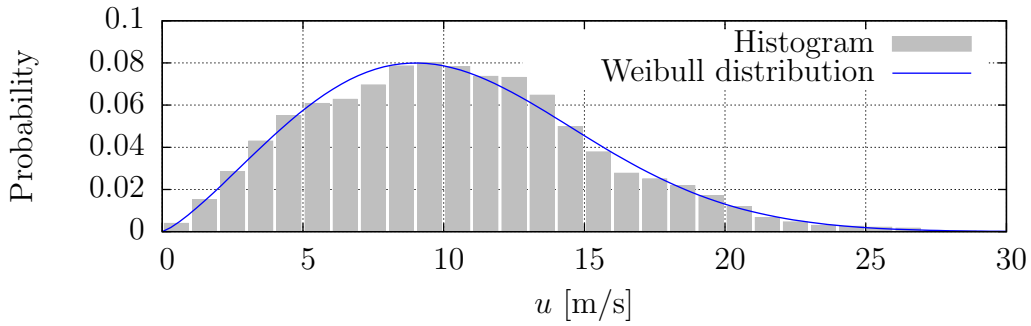


(a) 2011. $k = 2.256, A = 11.6699$

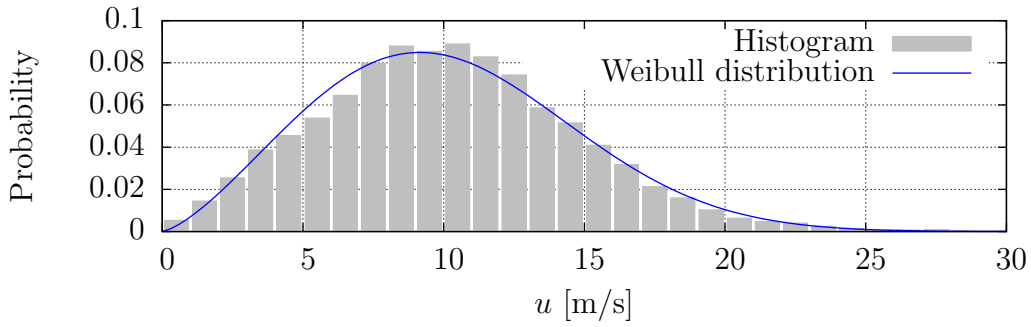


(b) 2012. $k = 2.391, A = 11.4819$

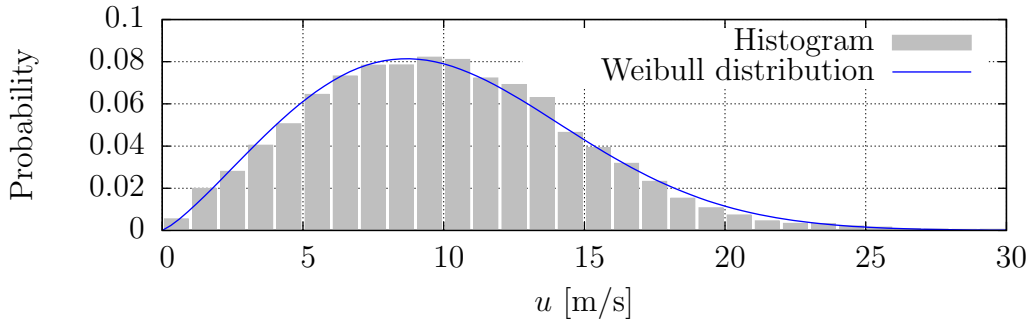


(c) 2013. $k = 2.2256, A = 11.3477$

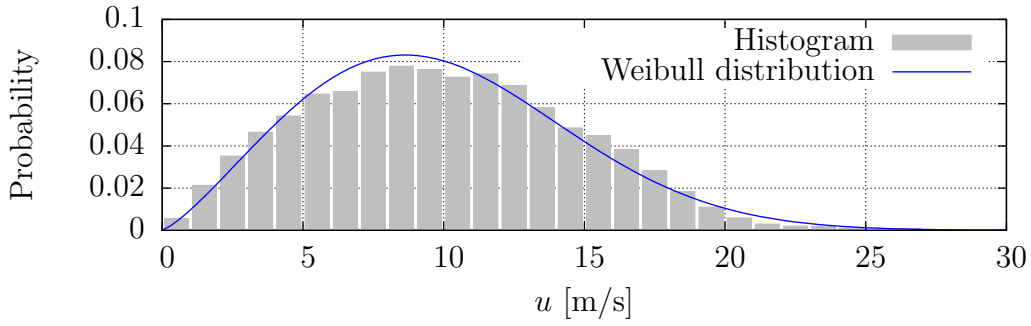


(d) 2014. $k = 2.2515, A = 11.209$

Figure 4: Direction independent wind speed distributions at FINO3 for the years 2011 to 2014

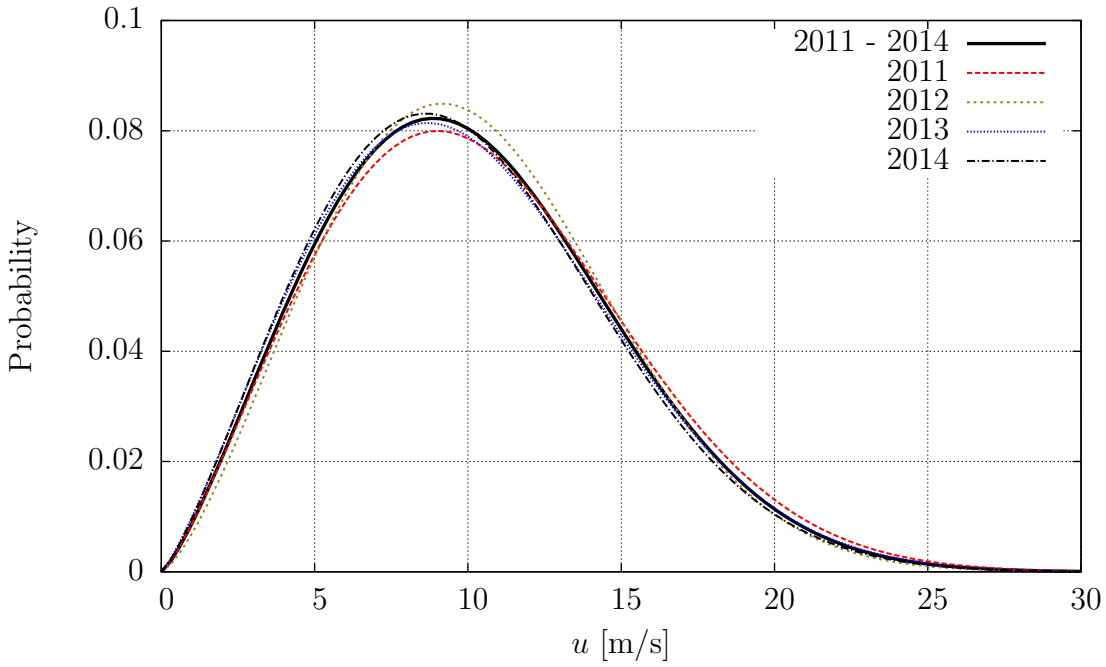


Figure 5: Comparison of annual wind speed distributions at FINO3 for the years 2011 to 2014

### 3.2.2 Quality of the Weibull fit for representing wind data

In the previous subsection we fitted the Weibull distribution to a set of measured wind speed values. Now we want to know if it is a good approximation for the given set of values. We therefore compare the quality of a Weibull fit to the quality of other distribution fits: Normal (Gaussian), Nakagami and Rice distribution.

As can be seen in the visual comparison of the PDFs with the histogram of clustered speed data in figure 6, the fitted Rice distribution is the most suitable representation of the measured data, followed by the Weibull distribution.

The graphical evaluation of quality with figure 6 may be wrong or at least imprecise as it strongly depends on the number of speed classes. Therefore, in figure 7 the root-mean-squared error (RMSE) for the four distribution fits concerning the clustered measured data is plotted for different numbers of speed classes. The RMSE of the Rice distribution is smaller than the RMSEs of the other distribution fits for all numbers of speed classes, which strengthens the observation from above. The oscillation effect of the curves in figure 7 for large numbers of speed classes comes from strongly varying fill of the speed classes which arise when the class widths get very small. With more measurements the oscillation would be reduced.

Figures 6 and 7 are based on measured data from FINO3 of the years 2011 to 2014. The dataset consists of more than 190 thousand values.

As another measurement for the fitting quality, which is independent of the cluster-

ing, we look at the Kolmogorov-Smirnov statistic [33]

$$D_n = \sup_x |F_n(x) - F(x)|, \tag{6}$$

where $F_n(x)$ denotes the empirical distribution function associated to the measured data, and $F(x)$ is the cumulative distribution function of the fitted distribution. The Kolmogorov-Smirnov statistics of the tested distributions are listed in table 2. The test again strengthens the observation that the Rice distribution is a better approximation for the measured wind data than the other considered distributions.

| **Distribution** | **Parameters** | **Kolmogorov-Smirnov statistic** |
|---|---|---|
| Normal distribution | $\mu = 10.1356,\ \sigma = 4.6967$ | 0.025051 |
| Nakagami distribution | $\mu = 1.21322,\ \omega = 124.789$ | 0.021663 |
| Weibull distribution | $A = 11.4322,\ k = 2.27993$ | 0.012846 |
| Rice distribution | $s = 7.96172,\ \sigma = 5.54079$ | 0.005770 |

Table 2: Quality of fitted distributions to measured wind data

In this thesis, the Weibull distribution is still used for describing the wind speed probabilities for the following reasons: The PDF of the Weibull distribution has a much simpler form than the PDF of the Rice distribution as it contains the Bessel function. Therefore it is also easier to fit the Weibull distribution. Furthermore the representation of the wind data using Weibull is common practice in wind farm modeling. Also the software Openwind, which is used for the verification of the models, needs the Weibull parameters for each direction sector as input.

Note that the normal distribution is only included into the tests for its popularity but in fact it is not eligible as it allows negative wind speeds, see figure 6.

As the here presented results are based on data of 4 years, they are probably also valid for different years and different sites in the North Sea. However for a good reliability of the wind data processing a similar test should be performed for each set of data.

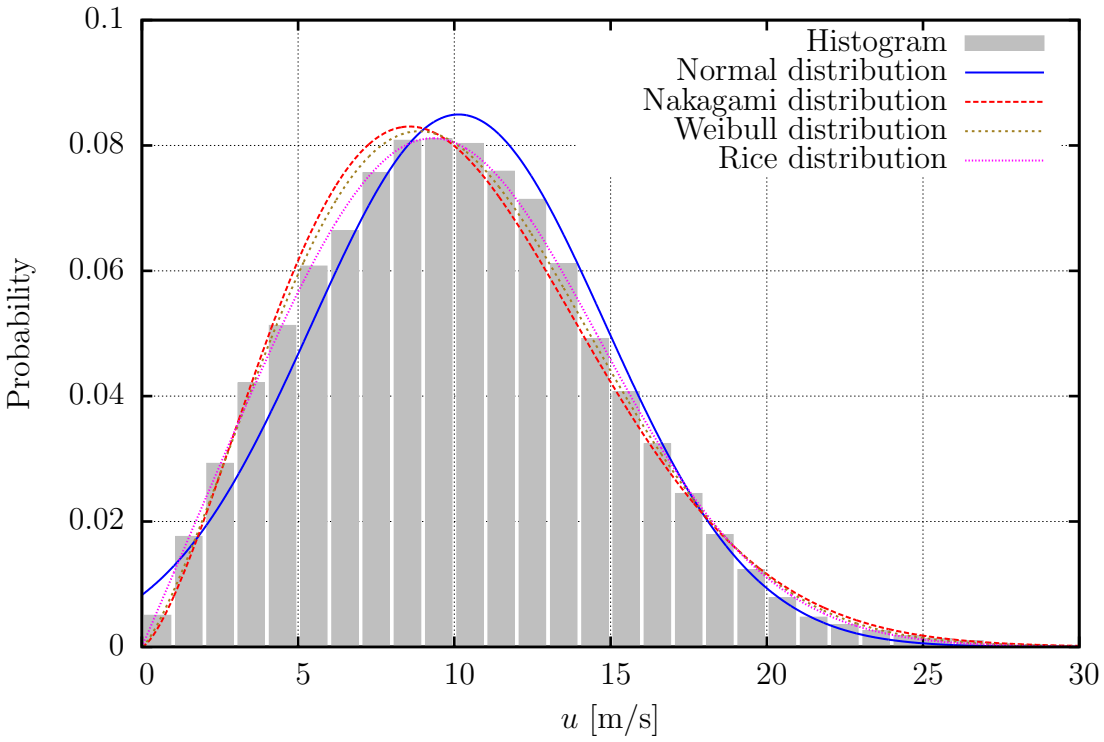


Figure 6: Comparison of probability density functions of distribution fits with clustered measured data

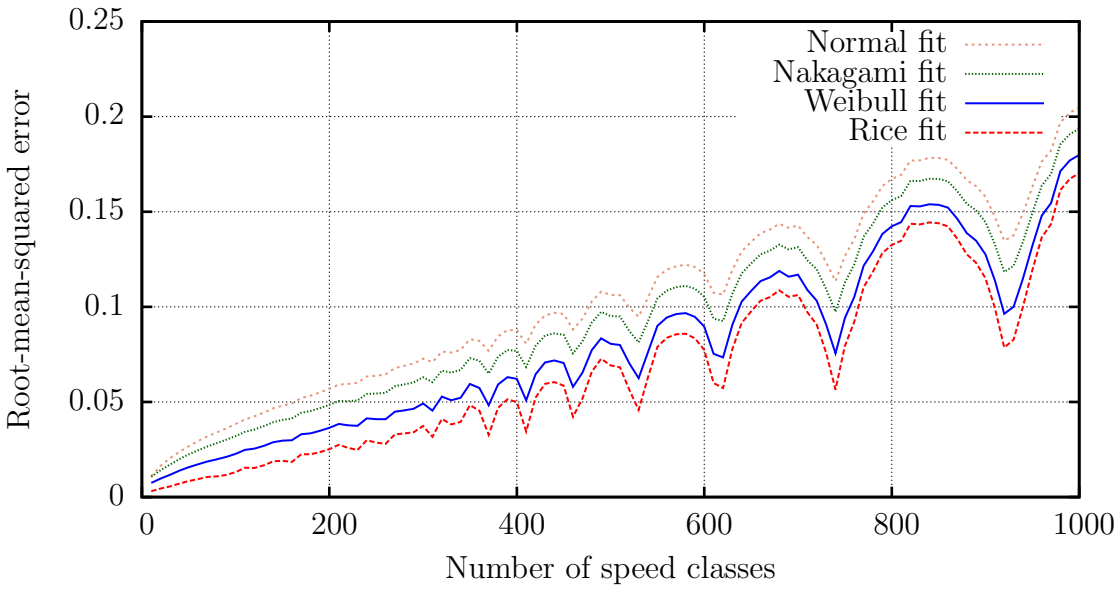


Figure 7: Root-mean-squared errors for distribution fits concerning clustered measured data

## 3.3 Annual energy production

The expected power value of a wind farm for all wind speeds $u$ in one wind direction $\varphi_i$ is given by

$$\begin{aligned} E_{\varphi_i} &:= E_{\varphi_i}\left[P(\varphi_i, u)\right] \\ &= \int_0^{\infty} P(\varphi_i, u) \cdot F_{\varphi_i}(u)\,\mathrm{d}u \\ &= \int_{u_{cutin}}^{u_{cutout}} P(\varphi_i, u) \cdot F_{\varphi_i}(u)\,\mathrm{d}u \\ &\approx \sum_{j=1}^{N_{speeds}} w_j \cdot P(\varphi_i, u_j) \cdot F_{\varphi_i}(u_j) \end{aligned} \tag{7}$$

where $F_{\varphi_i}(u)$ describes the PDF of the wind speed distribution, see 3.2, $u_{cutin}$ and $u_{cutout}$ are the turbines' cut-in and cut-out speed respectively, $w_j$ is the weight for speed class $j$ and

$$P(\varphi, u) = \sum_{k=1}^{N_{Turbines}} P(u_{inc,\varphi,k}) \tag{8}$$

denotes the total power output of the wind farm at wind speed $u$ and direction $\varphi$. $P(u)$ is the power production of one turbine at wind speed $u$ and $u_{inc,\varphi,k}$ is the incident wind speed at turbine $k$ at wind direction $\varphi$ and wind speed $u$. The incident speed is computed by

$$u_{inc} = (1 - \delta u)u_0, \tag{9}$$

where $u_0$ is the undisturbed free stream speed and

$$\delta u = \frac{u_0 - u_w}{u_0} = 1 - \frac{u_w}{u_0} \tag{10}$$

is the velocity deficit at the turbine rotor with disturbed wind speed $u_w$ inside another turbine's wake. The calculation of the velocity deficit is subject to the wake models described below.

The expected power value for all directions is

$$\begin{aligned} E &:= \int_0^{2\pi} E_{\varphi}\mathrm{d}\varphi \\ &\approx \sum_{i=1}^{N_{directions}} w_{\varphi_i} \cdot E_{\varphi_i} \end{aligned} \tag{11}$$

with $w_{\varphi_i}$ weight for direction $\varphi_i$.

As $E$ describes the mean power for a given wind distribution in MW, this must be projected to the length of one year to get the AEP measured in MWh:

$$\begin{aligned} AEP &= (8760\,\mathrm{h} + 6\,\mathrm{h}) \cdot E \\ &\approx (8760\,\mathrm{h} + 6\,\mathrm{h}) \cdot \sum_{i=1}^{N_{directions}} w_{\varphi_i} \cdot \sum_{j=1}^{N_{speeds}} w_j \cdot W_{\varphi_i}(u_j) \cdot \sum_{k=1}^{N_{Turbines}} P(u_{inc,\varphi_i,j,k}), \end{aligned} \quad (12)$$

with $u_{inc,\varphi_i,j,k}$ representing the incident velocity at turbine $k$, wind speed $u_j$ and wind direction $\varphi_i$. 8760 is the number of hours in a year and the additional six hours is a correction to get the mean number of hours per year with leap years respected. This complies to 365.25 days per year.

## 3.4 PARK wake model

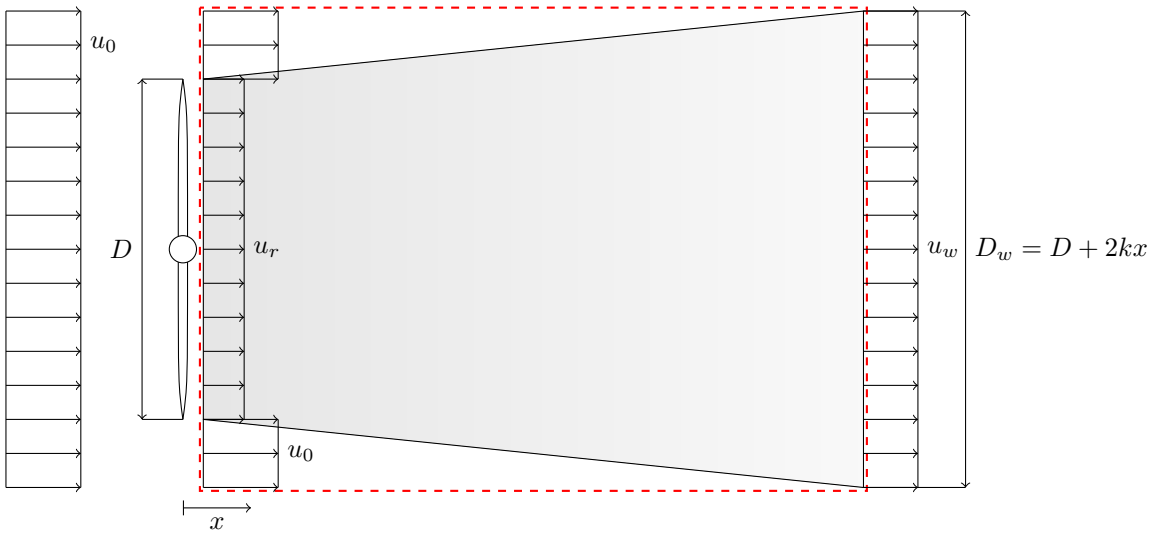


Figure 8: Visualization of the wake as described in PARK, cf. [21]

In this model, which was developed by Jensen [19] and Katic et al. [21], the velocity deficit inside the wake only changes in stream direction, i.e. the velocity deficit as defined in equation (10) only depends on $x$: $\delta u = \delta u(x)$. Therefore, it is not suitable for the calculation of a flow field with an exact velocity distribution. The model is designed for the far wake case, i.e. it is only valid for downstream distances of 3 rotor diameters or more. The wake radius grows with a factor $k$ so the wake diameter $D_w = D_w(x)$ grows linearly by $2k$, see figure 8. The scalar $k$ is defined as follows [34]:

$$k = \frac{0.5}{\ln \frac{z}{z_0}}, \quad (13)$$

where $z$ is the hub height of the turbine and $z_0$ is called surface roughness. The surface roughness is dependent on the site ground. It can be assumed as a constant

for most cases. There is a formula presented in [23] to compute the surface roughness dependent on the sea state based on the dependency of the waves on the wind velocity. Nevertheless, in this thesis we assume $z_0$ to be constant as the focus of the work is on the wake models. A typical value for offshore sites is 0.0002 m [8].

For the derivation of the velocity deficit inside a turbine's wake we assume conservation of momentum inside the wake and start with a balance of momentum

$$\sum mass \cdot velocity = \sum density \cdot area \cdot velocity = 0 \tag{14}$$

around the system shown in figure 8 (red, dashed box). Assuming incompressibility we get

$$-\rho\pi\left(\frac{D}{2}\right)^2 u_r - \rho\pi\left(\left(\frac{D_w}{2}\right)^2 - \left(\frac{D}{2}\right)^2\right) u_0 + \rho\pi\left(\frac{D_w}{2}\right)^2 u_w = 0, \tag{15}$$

which can be simplified to

$$D^2 u_r + \left(D_w^2 - D^2\right) u_0 = D_w^2 u_w. \tag{16}$$

Placing the initial velocity deficit right behind the turbine $\delta u_r = 1 - \frac{u_r}{u_0}$ in (16) and solving for $\frac{u_w}{u_0}$ yields

$$\frac{u_w}{u_0} = 1 - \delta u_r \left(\frac{D}{D + 2kx}\right)^2. \tag{17}$$

Replacing the initial velocity deficit $\delta u_r$ by the axial induction factor, which is defined as the relative velocity loss at the turbine[2] [15].

$$a(u_0) = 1 - \sqrt{1 - C_t(u_0)} \tag{18}$$

gives us the final equation for the velocity deficit at any point inside the wake of a turbine inside the free stream with velocity $u_0$.

$$\delta u(x) = 1 - \frac{u_w(x)}{u_0} = \frac{1 - \sqrt{1 - C_t(u_0)}}{\left(1 + \frac{2kx}{D}\right)^2}. \tag{19}$$

As the above derivation is only valid for the wake of a turbine in the free stream, we now want to generalize it to get the velocity deficit at a turbine inside the wake of another turbine that is not necessarily inside the free stream. A few things have to be changed so the above requirements are met: We call the wake generating turbine $i$ and the wake affected turbine $j$. The incident velocity of turbine $i$ then is $u_{inc,i}$. If turbine $j$ is fully affected by the wake, we can use the above formulation. However if

[2] The definition of the axial induction factor in Katic et al. [21] is not consistent with the derivation of the velocity deficit. The here used definition of the induction factor (18) is taken from Peña and Rathmann [28], assuming that $a = \delta u_r = 2a_{Katic}$. This way we can derive formula (19) for the velocity deficit as it is frequently used in literature, e.g. [10, 12, 22, 40, 41].

turbine $j$ is only partially affected, we need to introduce a shadowing factor $\beta_k \in [0,1]$ as presented in [7] and [37]:

$$\beta_k = \frac{A_{Intersection}}{A_{Turbine}}, \tag{20}$$

where $A_{Intersection}$ is the circular intersection of the wake cross section with the turbine's circular area $A_{Turbine}$, see figure 9. The equation for the velocity deficit has changed as follows:

$$1 - \frac{u_w}{u_{inc,i}} = \frac{\beta_k \left(1 - \sqrt{1 - C_t(u_{inc,i})}\right)}{\left(1 + \frac{2kx}{D}\right)^2}. \tag{21}$$

As this formulation depends on the incident velocity at turbine $i$, we need to transform it to make it dependent on the free stream velocity $u_0$:

$$\delta u_{ij} = 1 - \frac{u_{w,i}}{u_0} = 1 - \frac{u_{inc,j}}{u_0} = \frac{u_0}{u_{inc,i}} \left( \frac{\beta_k \left(1 - \sqrt{1 - C_t(u_{inc,i})}\right)}{\left(1 + \frac{2kx}{D}\right)^2} \right). \tag{22}$$

For the case of two interacting wakes the velocity deficits are added as follows:

$$\begin{aligned} \delta u_j^2 &= \delta u_{1,j}^2 + \delta u_{2,j}^2 \\ \Leftrightarrow \left(1 - \frac{u_{inc,j}}{u_0}\right)^2 &= \left(1 - \frac{u_{w,1}}{u_0}\right)^2 + \left(1 - \frac{u_{w,2}}{u_0}\right)^2, \end{aligned} \tag{23}$$

with $u_{w,1}$ and $u_{w,2}$ representing the velocities inside the two wakes. In a more general case with an arbitrary number of interacting wakes we can compute

$$\delta u_j = \sqrt{\sum_{i=1}^{N} \delta u_{ij}^2}, \tag{24}$$

where $N$ is the number of interacting wakes and $\delta u_{ij}$ represents the velocity deficits of the single wakes $i$ affecting turbine $j$.

In Openwind the resulting velocity deficit for wake intersections is not combined from the single wake velocity deficits but complies with the largest single wake deficit:

$$\delta u_j = \max_{i=1,\dots,N} (\delta u_{i,j}) \tag{25}$$

This equation must be used instead of (24) when validating the wake model with Openwind, see section 5.

## 3.5 Modified PARK wake model

The modified PARK model [37] introduces only small changes to the original PARK model. The intersection factor $\beta_k$ is calculated in one dimension and complies with the ratio between the radial distance and the rotor diameter $D$, see figure 9. Furthermore,

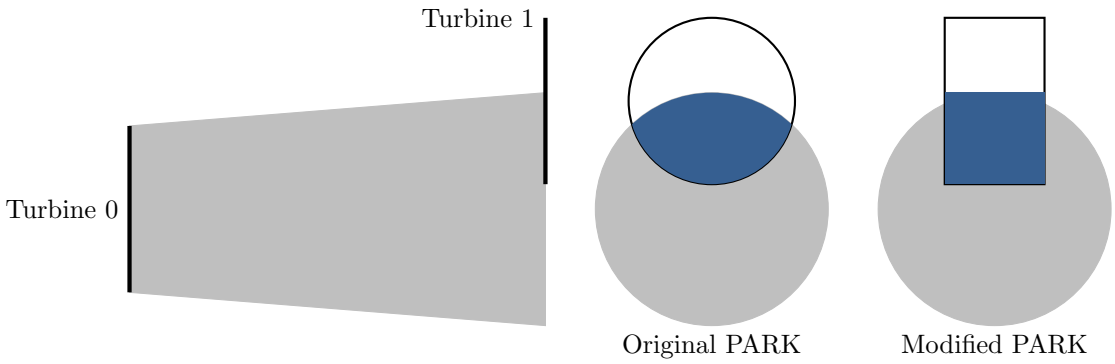


Figure 9: Calculation of the shadowing factor $\beta_k$ in original and modified PARK, cf. [37]

the velocity deficit calculated by equation (19) always depends on the free stream velocity instead of the incident velocity at the wake generating turbine. Only the thrust coefficient $C_t$ depends on the incident velocity. Equation (22) changes as follows:

$$\delta u_{ij} = 1 - \frac{u_{w,i}}{u_0} = \frac{\beta_k \left(1 - \sqrt{1 - C_t(u_{inc,i})}\right)}{\left(1 + \frac{2kx}{D}\right)^2}. \tag{26}$$

The above modifications lead to lower wake losses compared to those expected by the original PARK model.

## 3.6 Eddy-Viscosity wake model

The model introduced by Ainslie [1] in 1988 is based on the numerical solution of the thin shear layer approximation of the NS equations. It is assumed, that the wake is axisymmetric, fully turbulent and has no circumferential velocities. The flowfield is assumed to be stationary in time and the pressure gradients outside the wake to be negligible.

The momentum equation with the above assumptions is

$$u\frac{\partial u}{\partial x} + v\frac{\partial u}{\partial r} = -\frac{1}{r}\frac{\partial \left(r\overline{uv}\right)}{\partial r} \tag{27}$$

with $u$ velocity in downstream direction ($x$) and $v$ velocity in radial direction ($r$). The shear stresses are expressed by an eddy viscosity turbulence closure

$$-\overline{uv} = \varepsilon\frac{\partial u}{\partial r}, \tag{28}$$

with $\varepsilon$ eddy viscosity as described below. Placing (28) in (27) and applying the product rule yields

$$u\frac{\partial u}{\partial x} + v\frac{\partial u}{\partial r} = \frac{\varepsilon}{r}\left(\frac{\partial u}{\partial r} + r\frac{\partial^2 u}{\partial r^2}\right). \tag{29}$$

### 3.6.1 Eddy viscosity turbulence closure

The definition of the eddy viscosity is composed of the wake generated eddy viscosity and the ambient eddy viscosity

$$\varepsilon = l_w(x)\, u_w(x) + \varepsilon_a, \tag{30}$$

where $l_w$ is a characteristic length proportional to the wake width $r_w$, which is defined as[3]

$$r_w = \sqrt{\frac{3.56 C_t}{4\delta u_c\,(2 - \delta u_c)}} \cdot D, \tag{31}$$

$u_w$ is a characteristic velocity corresponding to the velocity difference $u_0 - u_c$ with $u_0$ free-stream velocity and $u_c$ centerline velocity inside the wake. Both $l_w$ and $u_w$ depend on the downstream distance $x$. With the given proportionality we can write

$$l_w(x)\, u_w(x) = k_l r_w(x)(u_0 - u_c(x)) \tag{32}$$

where $k_l$ is a proportionality factor, which was estimated by Ainslie to be 0.015. The ambient eddy viscosity $\varepsilon_a$ can be replaced by the eddy diffusivity which is defined for neutral conditions as

$$\varepsilon_a = K_M = \frac{\kappa^2}{\log\left(\frac{z}{z_0}\right)} u_0 D \tag{33}$$

with $\kappa$ von Kármán constant, $z_0$ surface roughness of the site and $z$ the height above the ground, which complies to the turbine hub height. The eddy diffusivity is a measure for the diffusion due to eddies inside the flow.

After wind tunnel experiments the eddy viscosity is lower than expected from the equations for downstream distances smaller than 5 rotor diameters. Therefore Ainslie introduced a filter function

$$F(x) = \begin{cases} 0.65 + \left(\frac{x/D - 4.5}{23.32}\right)^{1/3} & x \leq 5.5\, D \\ 1 & x > 5.5\, D \end{cases}, \tag{34}$$

which gives us the final equation for the eddy viscosity[4]

$$\varepsilon = F(x) \left( k_l r_w(x)(u_0 - u_c(x)) + \frac{\kappa^2}{\log\left(\frac{z}{z_0}\right)} u_0 D \right). \tag{35}$$

The slope of the original filter function at $x = 4.5D$ is infinite. This leads to a leap in the distribution of $v$, see figure 10a. As this leads to a leap in the eddy viscosity at this point, some modifications for $F(x)$ are introduced, see figure 11. One approach is

[3] In literature this is called wake width, although it is a measure for the wake radius. See [1], [37]

[4] After [23] the filter function is not applied to the ambient eddy viscosity.

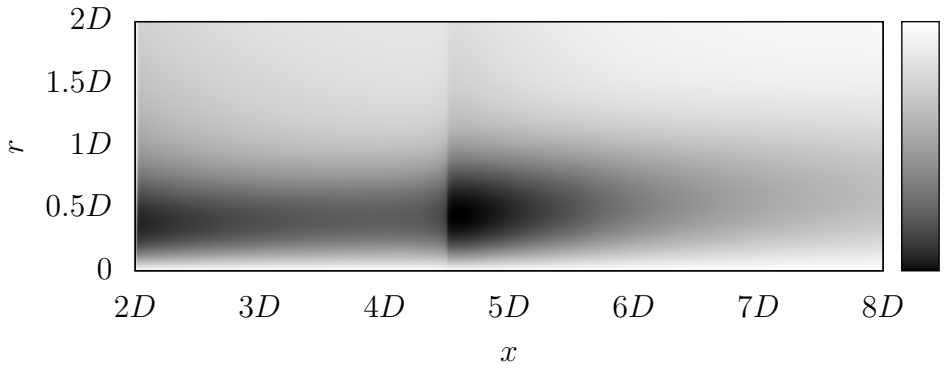


(a) Original filter function, see equation (34)

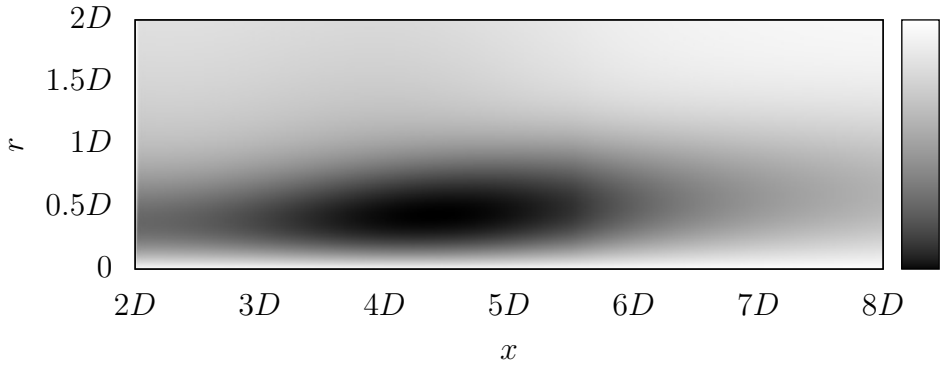


(b) Exponential filter function, see equation (37)

Figure 10: Comparison of radial speed distributions with different filter functions

to replace the critical part of the function by a linear function around $x = 4.5D$ with a more moderate slope:

$$F_{lin}(x) = \begin{cases} F(x) & x \leq 4.1\,D \text{ or } x \geq 4.9\,D \\ \frac{F(4.9D)-F(4.1D)}{0.8D}\,(x - 4.9D) + F(4.9D) & 4.1\,D < x < 4.9\,D \end{cases} \tag{36}$$

Another idea is to take another S-shaped function similar to the original one. Here, an exponential function and the cumulative distribution function (CDF) of the normal distribution were fitted to the characteristic points at $x = \{0,\, 4.5,\, 5.5\}$, giving

$$F_{exp}(x) = \begin{cases} \frac{1.16004}{1+\exp(1.39713\cdot(4.5-x/D))} + 0.069979 & x \leq 5.5\,D \\ 1 & x > 5.5\,D \end{cases} \quad \text{and} \tag{37}$$

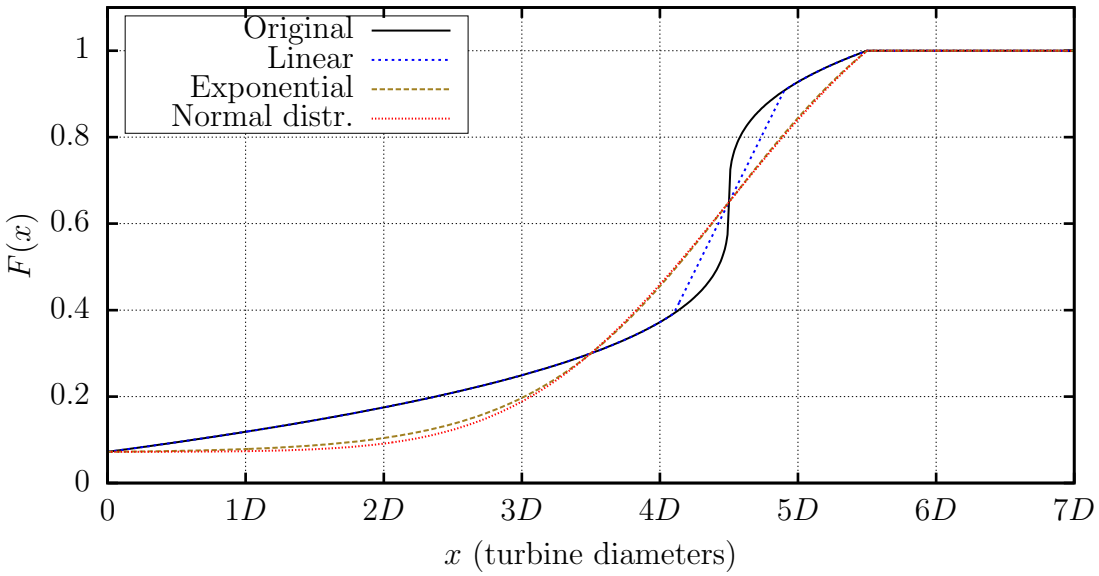


Figure 11: Filter function $F(x)$ for the eddy viscosity in the near-wake with variations

$$F_{normal}(x) = \begin{cases} 1.15588 \cdot \underbrace{\left[\frac{1}{2}\left(1 + \operatorname{erf}\left(\frac{x/D - \mu}{\sqrt{2\sigma^2}}\right)\right)\right]}_{\text{CDF of } \mathcal{N}(\mu,\sigma^2)} + 0.0720596 & x \leq 5.5\,D \\ 1 & x > 5.5\,D \end{cases} \tag{38}$$

with $\mu = 4.5$ and $\sigma = 1.1740957$. As can be seen on figure 11 the exponential approach is a slightly better approximation to the original filter function. Exemplary for the modified filter functions, the distribution of $v$ when using the exponential filter function $F_{exp}(x)$ is plotted in figure 10b. Note that the physical quality of the above equations was not tested. The modifications are proposals for getting a smoother course for the eddy viscosity $\varepsilon$.

### 3.6.2 Discretization

We now want to solve the partial differential equation (PDE) (29) numerically using finite differences. Therefore, the approach given in literature ([13]. [37]) is used. We first discretize the radial direction and understand $x$ as a time variable, since the problem is assumed to be stationary and the flow evolves in downstream direction. This way we get a set of ordinary differential equations (ODEs) which can be solved by the below methods.

For each discretization step in $x$ a linear system of equations is set up and solved for the velocity at that $x$.

Equation (29) has a singularity at $r = 0$. By multiplying by $r$ we get

$$ru\frac{\partial u}{\partial x} + vr\frac{\partial u}{\partial r} = \varepsilon\left(\frac{\partial u}{\partial r} + r\frac{\partial^2 u}{\partial r^2}\right). \tag{39}$$

Placing $r = 0$ in this equation gives the following condition for the solution:

$$\varepsilon\frac{\partial u}{\partial r} = 0 \tag{40}$$

As $\varepsilon$ is non-zero, the radial derivative must equal zero at the wake centerline ($r = 0$). This condition complies with our assumption of radial-symmetry.

For solving the given PDE, equation (29) is again slightly rearranged before discretizing:

$$u\frac{\partial u}{\partial x} = \left(\frac{\varepsilon}{r} - v\right)\frac{\partial u}{\partial r} + \varepsilon\frac{\partial^2 u}{\partial r^2} \tag{41}$$

Now the derivatives with respect to $r$ are discretized using central differences

$$\begin{aligned}\frac{\partial u}{\partial r} &= \frac{u_{i+1} - u_{i-1}}{2\Delta r}\\ \frac{\partial^2 u}{\partial r^2} &= \frac{u_{i+1} - 2u_i + u_{i-1}}{(\Delta r)^2}.\end{aligned} \tag{42}$$

This gives a set of ODEs which can then be solved numerically using one of the below methods.

**Backward Euler discretization scheme** The backward Euler method is a one-sided finite differences scheme which can be used for flow problems in flow direction. Applying on equation (29) yields

$$u_{i,j}\frac{u_{i,j+1} - u_{i,j}}{\Delta x} = \left(\frac{\varepsilon_j}{r_i} - v_{i,j}\right)\frac{u_{i+1,j+1} - u_{i-1,j+1}}{2\Delta r} + \varepsilon_j\frac{u_{i+1,j+1} - 2u_{i,j+1} + u_{i-1,j+1}}{(\Delta r)^2}. \tag{43}$$

After multiplying by $2r_i\Delta x(\Delta r)^2$ and sorting by the velocities at $j+1$ we get

$$\begin{aligned}&\left(\Delta x\Delta r\varepsilon_j - r_i\Delta x\Delta r v_{i,j} - 2\varepsilon_j r_i\Delta x\right)u_{i-1,j+1}\\ &+ \left(2r_i u_{i,j}(\Delta r)^2 + 4\varepsilon_j r_i\Delta x\right)u_{i,j+1}\\ &+ \left(r_i\Delta x\Delta r v_{i,j} - \Delta x\Delta r\varepsilon_j - 2\varepsilon_j r_i\Delta x\right)u_{i+1,j+1}\\ &= 2r_i(\Delta r)^2 u_{i,j}^2\end{aligned} \tag{44}$$

with $i = 1, ..., n-1$. The boundary $i = 0$ is treated in 3.6.3. (44) can be expressed by

$$a_i u_{i-1,j+1} + b_i u_{i,j+1} + c_i u_{i+1,j+1} = d_i, \tag{45}$$

where

$$\begin{aligned}a_i &= \Delta x\left(\Delta r\varepsilon_j - r_i\Delta r v_{i,j} - 2\varepsilon_j r_i\right),\\ b_i &= 2r_i\left(u_{i,j}(\Delta r)^2 + 2\varepsilon_j\Delta x\right),\\ c_i &= \Delta x\left(r_i\Delta r v_{i,j} - \Delta r\varepsilon_j - 2\varepsilon_j r_i\right) \text{ and}\\ d_i &= 2r_i(\Delta r)^2 u_{i,j}^2.\end{aligned} \tag{46}$$

**Crank-Nicolson discretization scheme** The Crank-Nicolson scheme is based on the trapezoidal rule. It is a combination of the forward and the backward Euler methods.

$$\begin{aligned} u_{i,j}\frac{u_{i,j+1}-u_{i,j}}{\Delta x} &= \frac{1}{2}\left(\frac{\varepsilon_j}{r_i}-v_{i,j}\right)\left(\frac{u_{i+1,j+1}-u_{i-1,j+1}}{2\Delta r}+\frac{u_{i+1,j}-u_{i-1,j}}{2\Delta r}\right) \\ &\quad+\frac{\varepsilon_j}{2}\left(\frac{u_{i+1,j+1}-2u_{i,j+1}+u_{i-1,j+1}}{(\Delta r)^2}+\frac{u_{i+1,j}-2u_{i,j}+u_{i-1,j}}{(\Delta r)^2}\right) \end{aligned} \tag{47}$$

The discretized formulation in equation (47) is multiplied by $4r_i\Delta x(\Delta r)^2$ and sorted by the velocities at $j+1$ so we get

$$\begin{aligned} &\left(\varepsilon_j\Delta x\Delta r - r_i v_{i,j}\Delta x\Delta r - 2\varepsilon_j r_i\Delta x\right)u_{i-1,j+1} \\ &+\left(4r_i u_{i,j}(\Delta r)^2+4\varepsilon_j r_i\Delta x\right)u_{i,j+1} \\ &+\left(r_i v_{i,j}\Delta x\Delta r-\varepsilon_j\Delta x\Delta r-2\varepsilon_j r_i\Delta x\right)u_{i+1,j+1} \\ &=4r_i(\Delta r)^2u_{i,j}^2+\left(\varepsilon_j\Delta x\Delta r-r_i v_{i,j}\Delta x\Delta r\right)\left(u_{i+1,j}-u_{i-1,j}\right) \\ &+2\varepsilon_j r_i\Delta x\left(u_{i+1,j}-2u_{i,j}+u_{i-1,j}\right). \end{aligned} \tag{48}$$

Analogous to equation (45) this is expressed by

$$a_i u_{i-1,j+1}+b_i u_{i,j+1}+c_i u_{i+1,j+1}=d_i, \tag{49}$$

with

$$\begin{aligned} a_i &= \Delta x\left(\varepsilon_j\Delta r-r_i v_{i,j}\Delta r-2\varepsilon_j r_i\right), \\ b_i &= 4r_i\left(u_{i,j}(\Delta r)^2+\varepsilon_j\Delta x\right), \\ c_i &= \Delta x\left(r_i v_{i,j}\Delta r-\varepsilon_j\Delta r-2\varepsilon_j r_i\right) \text{ and} \\ d_i &= 4r_i(\Delta r)^2u_{i,j}^2+\left(\varepsilon_j\Delta x\Delta r-r_i v_{i,j}\Delta x\Delta r\right)\left(u_{i+1,j}-u_{i-1,j}\right) \\ &\quad+2\varepsilon_j r_i\Delta x\left(u_{i+1,j}-2u_{i,j}+u_{i-1,j}\right). \end{aligned} \tag{50}$$

**Setting up the matrix system** Equation (45) or (49) respectively can be written as matrix equation

$$A\underline{u}=\underline{d} \tag{51}$$

with

$$A=\begin{bmatrix} b_0 & c_0^* & 0 & \cdots & 0 \\ a_1 & b_1 & c_1 & & \vdots \\ 0 & \ddots & \ddots & \ddots & 0 \\ \vdots & & a_{n-2} & b_{n-2} & c_{n-2} \\ 0 & \cdots & 0 & a_{n-1} & b_{n-1} \end{bmatrix},\quad \underline{u}=\begin{bmatrix} u_{0,j+1} \\ u_{1,j+1} \\ \vdots \\ u_{n-2,j+1} \\ u_{n-1,j+1} \end{bmatrix},\quad \underline{d}=\begin{bmatrix} d_0 \\ d_1 \\ \vdots \\ d_{n-2} \\ d_{n-1}^* \end{bmatrix}. \tag{52}$$

As $v_{i,j}$ is required for solving the set of equations, another equation is needed. The continuity equation is therefore used and discretized with the upwind discretization

scheme [37].

$$\begin{aligned} & \frac{\partial u}{\partial x} + \frac{1}{r}\frac{\partial (rv)}{\partial r} = 0 \\ \Leftrightarrow \quad & \frac{\partial u}{\partial x} + \frac{\partial v}{\partial r} + \frac{v}{r} = 0 \\ \Leftrightarrow \quad & v = -r\left(\frac{\partial u}{\partial x} + \frac{\partial v}{\partial r}\right) \end{aligned} \tag{53}$$

$$\begin{aligned} & v_{i,j} = -r_i\left(\frac{v_{i,j} - v_{i-1,j}}{\Delta r} + \frac{u_{i,j} - u_{i,j-1}}{\Delta x}\right) \\ \Leftrightarrow \quad & v_{i,j} = \frac{r_i}{\Delta r + r_i}\left(v_{i-1,j} - \frac{\Delta r}{\Delta x}\left(u_{i,j} - u_{i,j-1}\right)\right) \\ & = \frac{i}{1+i}\left(v_{i-1,j} - \frac{\Delta r}{\Delta x}\left(u_{i,j} - u_{i,j-1}\right)\right) \end{aligned} \tag{54}$$

### 3.6.3 Boundary conditions

From equation (40) we know that $\frac{\partial u}{\partial r}$ is zero at the wake centerline and we get

$$u\frac{\partial u}{\partial x}\bigg|_{r=0} = \varepsilon\frac{\partial^2 u}{\partial r^2}. \tag{55}$$

Discretizing this simplified equation of momentum with the Crank-Nicolson discretization scheme yields the coefficients for the equation system (51) stated in equation (56). Using the backward Euler scheme yields equation (57).

$$\begin{aligned} a_0 &= -\varepsilon_j \Delta x \\ b_0 &= 2u_{0,j}(\Delta r)^2 + 2\varepsilon_j \Delta x \\ c_0 &= a_0 = -\varepsilon_j\, \Delta x \\ d_0 &= 2u_{0,j}^2(\Delta r)^2 + \varepsilon_j \Delta x(u_{1,j} - 2u_{0,j} + u_{-1,j}) \\ &= 2u_{0,j}^2(\Delta r)^2 + 2\varepsilon_j \Delta x(u_{1,j} - u_{0,j}) \end{aligned} \tag{56}$$

$$\begin{aligned} a_0 &= -\varepsilon_j \Delta x \\ b_0 &= u_{0,j}(\Delta r)^2 + 2\varepsilon_j \Delta x \\ c_0 &= a_0 = -\varepsilon_j \Delta x \\ d_0 &= u_{i,j}^2(\Delta r)^2 \end{aligned} \tag{57}$$

With the symmetry around $r = 0$ we have $u_{i-1,j+1} = u_{i+1,j+1}$ and thus

$$c_0^* = c_0 + a_0 = 2a_0. \tag{58}$$

For the outer wake border the velocity complies with the free stream velocity $u_0$. We can move $c_{n-1}u_0$ to the right-hand side and get

$$d_{n-1}^* = d_{n-1} - c_{n-1}u_0. \tag{59}$$

As the wake develops in downstream direction it can be divided into different regions. The near wake region is the region directly behind the rotor, which is dominated by pressure gradients and has the length $x_n$, which was fixed by Ainslie to $2D$. The EV wake model is only defined for downstream distances of more than $2D$.

The distribution of the velocity deficit at the transition between near wake and far wake at $x = x_n$ is assumed to be Gaussian with its peak at the centerline of the wake

$$1 - \frac{u_{c,n}}{u_{inc}} = C_t - 0.05 - (16C_t - 0.5)\,\frac{I_a}{10}. \tag{60}$$

For an initial centerline velocity deficit $\delta u_{c,n}$ with respect to the ambient wind speed $u_0$ we transform this equation and get

$$\delta u_{c,n} = 1 - \frac{u_{c,n}}{u_0} = 1 + \frac{u_{inc}}{u_0}\left(C_t - 0.05 - (16C_t - 0.5)\,\frac{I_a}{10} - 1\right). \tag{61}$$

The wake width at $x = x_n$ is then calculated using equation (31) with $\delta u_c = \delta u_{c,n}$ and the velocity deficit for any $r$ is given by

$$\delta u(x_n, r) = \delta u_{c,n} \mathrm{e}^{\left(-3.56\left(\frac{r}{r_w}\right)^2\right)}. \tag{62}$$

In addition to the boundary conditions for $u$ there are also boundary conditions for $v$ required. There is no radial velocity outside the wake and at the centerline. Therefore $v_{0,j}$ is set to 0. As the wake edge does not have influence on the calculation of $v$ there are no boundary conditions required for the outer wake border.

For the width of the cylindrical grid equation (31) is used. We set $\delta u_c$ to a sufficiently small number, e.g. 0.1 %, so we get the maximal wake width if the calculation is stopped for centerline velocity deficits lower than the provided number.

### 3.6.4 Solution

The matrix given in equation (52) is now tested for different properties to find a suitable solution algorithm. It can easily be seen that the matrix is in *tridiagonal* form.

At first, the matrix is tested for *diagonal dominance*. Therefore, the sum of all off-diagonal entries in a row must be lower than the diagonal entry. This must be checked for all lines, so we check the first line, which is set by the boundary condition, and an arbitrary line $i$ with $i \in [1, n-1]$: We start with backward Euler:

$$\begin{aligned} |a_i| + |c_i| &< |b_i| \\ 2\varepsilon_j \Delta x &< u_{i,j}(\Delta r)^2 + 2\varepsilon_j \Delta x \\ 0 &< u_{i,j}(\Delta r)^2 \end{aligned} \tag{63}$$

$$\begin{aligned} |a_0| + |c_0| &< |b_0| \\ 2\varepsilon_j \Delta x &< u_{0,j}(\Delta r)^2 + 2\varepsilon_j \Delta x \end{aligned}$$

$$0 < u_{0,j}(\Delta r)^2 \tag{64}$$

Now we do the same for Crank-Nicolson:

$$\begin{aligned} |a_i| + |c_i| &< |b_i| \\ \varepsilon_j \Delta x &< u_{i,j}(\Delta r)^2 + \varepsilon_j \Delta x \\ 0 &< u_{i,j}(\Delta r)^2 \end{aligned} \tag{65}$$

$$\begin{aligned} |a_0| + |c_0| &< |b_0| \\ 2\varepsilon_j \Delta x &< u_{0,j}(\Delta r)^2 + 2\varepsilon_j \Delta x \\ 0 &< u_{0,j}(\Delta r)^2 \end{aligned} \tag{66}$$

This shows that the matrix that is set up by both methods is diagonally dominant with the assumption that $u > 0$ holds.

In the next step, the matrix is tested for *irreducibility*. A tridiagonal matrix is irreducible if the entries of the secondary diagonals are non-zero. This can't be shown for the considered matrix.

As we also cannot show symmetry the matrix is not symmetric positive-definite.

Therefore, the most suitable solvers are the Thomas algorithm for tridiagonal matrices [30], which solves the system directly in $\mathcal{O}(n)$, and the Gaussian elimination method.

### 3.6.5 Wake generated turbulence

Until now, only the velocity loss inside the wake was considered. But with the deficit in velocity the turbulence intensity increases, so this should also be respected in the wake model. The effect is implemented as an extension for the EV model in [13] and [37]. The calculation of the turbulence intensity inside the wake is as follows: The provided equation from [37] for the wake-induced turbulence intensity is

$$I_w = 5.7 C_t^{0.7} I_a^{0.68} \left(\frac{x}{x_n}\right)^{-0.96}, \tag{67}$$

where $x_n$ is the near-wake length as given below and $\frac{x}{x_n}$ must not be lower than 1.5. The total turbulence intensity at a rotor inside another turbine's wake is then

$$I_{tot} = \frac{u_0}{u_{inc}} \sqrt{\beta_k I_w^2 + I_a^2} \tag{68}$$

with $\beta_k$ the shadowing factor as given in the PARK model, see equation (20). The wake width for the calculation of $\beta_k$ is twice the Eddy-Viscosity wake width $2\,r_w$.

The near-wake length $x_n$ is calculated as follows:

After Vermeulen [39] the near wake region can be separated into two sub-regions whereof the first has a length

$$x_h = r_r \left[ \left(\frac{dr}{dx}\right)_a^2 + \left(\frac{dr}{dx}\right)_\lambda^2 + \left(\frac{dr}{dx}\right)_m^2 \right]^{-1/2} \tag{69}$$

with $r_r$ effective radius of the fully expanded rotor disc as defined in [39]

$$r_r = \frac{D}{2}\sqrt{\frac{m+1}{2}} \quad \text{with } m = \frac{u_0}{u_r} = \frac{1}{\sqrt{1-C_t}}, \tag{70}$$

$u_r$ denotes the velocity directly behind the rotor, and the turbulence contributions describing the ambient, the rotor-generated and the shear-generated turbulence

$$\begin{aligned}
\left(\frac{dr}{dx}\right)_a &= \begin{cases} 2.5I_a + 0.05 & I_a \geq 0.02 \\ 5I_a & I_a < 0.02 \end{cases} \\
\left(\frac{dr}{dx}\right)_\lambda &= 0.012B\lambda \\
\left(\frac{dr}{dx}\right)_m &= \frac{(1-m)\sqrt{1.49+m}}{9.76(1+m)}
\end{aligned} \tag{71}$$

where $B$ denotes the number of blades and $\lambda$ is the tip speed ratio

$$\lambda = \frac{RPM\,\pi D}{60 u_{inc}}. \tag{72}$$

$RPM$ is a velocity dependent turbine property (Revolutions per minute) and $u_{inc}$ the incident velocity of the wake generating turbine. The near-wake length then is

$$x_n = \frac{\sqrt{0.212+0.145m}}{1-\sqrt{0.212+0.145m}} \frac{1-\sqrt{0.134+0.124m}}{\sqrt{0.134+0.124m}} x_h. \tag{73}$$

Because of a singularity at $C_t = 0.97$, $C_t$ is set to 0.9 for the calculation of $x_n$ if it is greater than 0.9.

When calculating the turbulence intensity gain the new total turbulence intensity at a turbine is the incident turbulence intensity. It can be seen as the ambient turbulence intensity for this turbine. Therefore, the ambient turbulence intensity has to be replaced by the total turbulence in the description of the EV model.

### 3.6.6 Wake rotor intersections

To determine the incident speed at a turbine rotor the mean velocity deficit over the rotor area is calculated. This part of the model is not described in literature. The integral is therefore solved numerically using a quadrature rule such as Gaussian quadrature for the radial direction combined with the midpoint rule for the angle. The velocity deficits at the evaluation points are determined by bilinear interpolation between 4 grid points. As the velocity deficit is computed on a 2D grid and the wake rotor intersection is a 3D problem the grid needs to be rotated around the wake centerline to get a cylindrical 3D grid, see figure 12. A derivation for the mean velocity deficit is stated below.

$$\overline{\delta u} = \frac{1}{A(\Omega)} \int\int \delta u(x,y)\,\mathrm{d}\Omega$$

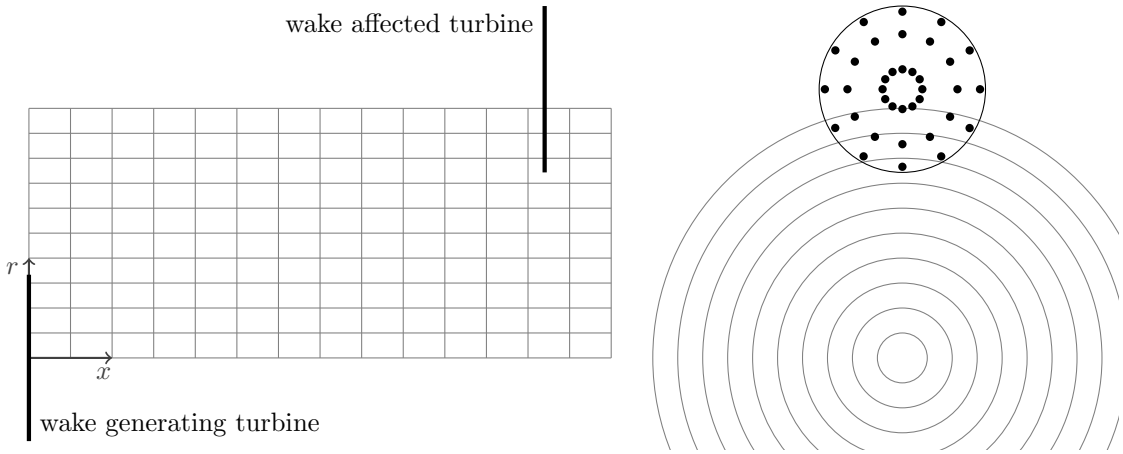


Figure 12: Wake turbine intersections in Eddy-Viscosity

$$
\begin{aligned}
&= \frac{1}{\pi R^2} \int_0^{2\pi} \int_0^{R} \delta u(r,\varphi)\, r \,\mathrm{d}r \,\mathrm{d}\varphi \\
&= \frac{1}{\pi R^2} \int_0^{\pi} \int_{-R}^{R} \delta u(r,\varphi)\, r \,\mathrm{d}r \,\mathrm{d}\varphi \\
&= \frac{1}{\pi R^2} \int_0^{\pi} 2R \sum_{i=1}^{N_r} w_i\, \delta u_i(\varphi)\, r_i \,\mathrm{d}\varphi \\
&= \frac{2}{\pi R} \pi \sum_{\alpha=1}^{N_\varphi} w_\alpha \sum_{i=1}^{N_r} w_i\, \delta u_{i,\alpha}\, r_i \\
&= \frac{2}{R} \sum_{\alpha=1}^{N_\varphi} \sum_{i=1}^{N_r} w_{i,\alpha}\, \delta u_{i,\alpha}\, r_i
\end{aligned} \tag{74}
$$

where $\overline{\delta u}$ denotes the mean velocity deficit, $R$ is the rotor radius $\frac{D}{2}$, $N_r$ and $N_\varphi$ are the numbers of supporting points in radial direction and the number of angles respectively, $\Omega$ describes the circular rotor disk in a general formulation and $A(\Omega)$ denotes the area of $\Omega$. The incident speed is then

$$u_{inc} = u_0 \left(1 - \overline{\delta u}\right). \tag{75}$$

If more than one wake affects a grid point, equation (24) applies for velocity deficits at the evaluation points.

$$\delta u_j = \sqrt{\sum_{i=1}^{N} \delta u_{ij}^2} \tag{24 revisited}$$

## 3.7 Cost Model

As mentioned in section 2.2 there are some cost models of varying complexity. The cost model used in this thesis is the most simple one used for instance by Mosetti et al. [26]. It is assumed that the costs only depend on the number of turbines in the farm.

$$LCOE = \frac{C}{E_a}, \tag{76}$$

where $E_a$ is the annual energy production (AEP) and $C$ describes the costs

$$C = N\left(\frac{2}{3} + \frac{1}{3} \cdot e^{-0.00147N^2}\right). \tag{77}$$

This cost function could be used to optimize the number of turbines in a wind farm. For an optimization of the turbine type another model which respects different component costs of a wind farm would be required.

# 4 Software

## 4.1 Implementation

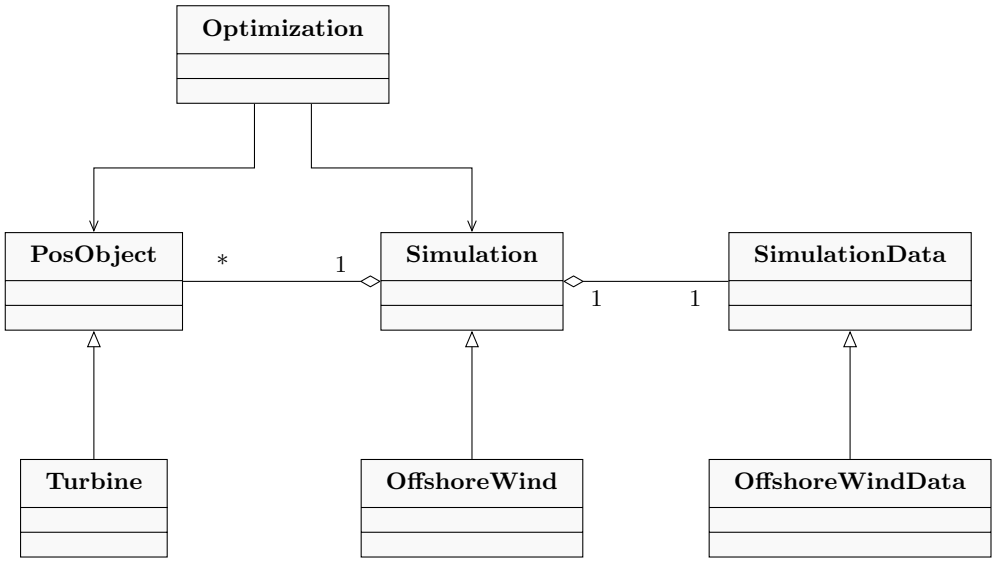


Figure 13: Class diagram

The models presented in section 3 are implemented in C++. The implementation is affiliated to an existing simulation and optimization framework that is used to optimize the heliostat field layout of solar tower power plants, see [17]. The employed optimization is a genetic algorithm (GA) specialized for optimizing two dimensional positions of objects. As the existing software is extensible the optimization can be applied to the newly implemented offshore wind farm simulation. A class diagram is shown in figure 13. The central class is the Simulation class, which includes the management of PosObjects (Turbines) and the simulation itself, which can be seen as an evaluation of the positions. The parameters and additional data are managed by the SimulationData class. Turbine, OffshoreWind and OffshoreWindData are specializations of the three previously mentioned classes respectively.

The parameters required for the simulation are provided using an INI-file, which is read by the SimulationData/OffshoreWindData class on initialization.

For the wake computations using the implemented models, the positions of the turbines are calculated in a rotated coordinate system such that the wind comes from $-x$ for each wind direction. The turbines are then sorted by their rotated $x$ coordinates so only the turbines with a lower $x$ coordinate need to be considered for the calculation of the incident speed at a turbine. Also the $y$ coordinate can then be used to easily find out if a turbine's wake affects another turbine.

## 4.2 Openwind

Openwind [2, 37] is a software developed by AWS Truepower for professional planning and analysis of wind farms. The implemented wake models are those presented in this thesis and the so-called Deep-Array Wake Model (DAWM), see [5]. Therefore Openwind is used for the verification of the during this work developed simulation code. The software is based on the geographic information system (GIS), i.e. the user interface and files are structured as map layers.

### 4.2.1 Input files

For the use of Openwind there are several files required:

- If it is desired to use one of the in Openwind predefined turbine types, a new turbine type needs to be created. One option is to enter the turbine properties manually in the user interface. Easier is loading a turbine file. Therefore an `xml` file with the extension `.owtg` is used.
- For the representation of wind data more than one file is used. Openwind can read wind resource grids (`.wrg` files) as used in the WAsP software, see [8]. This file format can specify more than only the wind distribution, also dimension such as surface roughness can be saved in wind resource grids.
- Additionally to the `.wrg` file a `.tab` file representing a met mast is required. The format of this file type is also provided in [8].
- Lastly the position of the met mast is fixed by loading a Point wind resource grid, which complies with a normal `.wrg` file but contains only one grid point.
- In the future it may be useful to also load `.asc` files. These are ESRI grids (ASCII grids), which can contain several different parameters such as surface roughness, elevation or maybe water depth. This can be helpful when extending the implementation.

For the verification of the models there were methods implemented to write and read the above file types.

# 5 Verification and results

In this section the procedures and results of the model verification are presented. In the last subsection 5.4 the presented model is used to simulate and optimize a real offshore wind farm.

## 5.1 Verification of the AEP computation

For testing the computation of the AEP, it is assumed that the wind comes from one direction with an artificial Weibull probability distribution. The annual energy production of one single turbine is calculated. Then different quadrature rules with varying number of points are tested against each other and against the results of Openwind. For a very simple case, where the power curve is set to a constant value of 1 MW, the integral can be computed analytically. The analytical solution is then used as a reference for the test.

### 5.1.1 One turbine, constant power curve, one wind direction

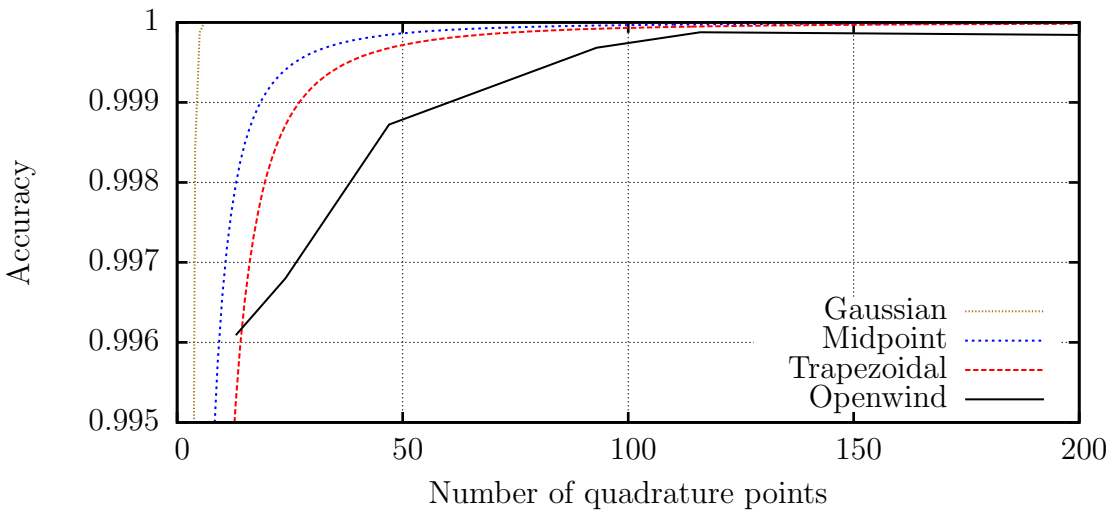


Figure 14: AEP verification: One turbine with a constant power curve and one wind direction

In this test the integral from equation (7) is solved numerically. The turbine type used for this test is Enercon E-82, see figure 2, with a cut-in speed of 2 m/s and a cut-out speed of 25 m/s but the power curve is replaced by a constant value of $P(\varphi_i, u) \equiv 1\,\text{MW}$. The tested integration methods are the trapezoidal rule, the midpoint rule and the Gaussian quadrature rule. The results are then compared to the exact solution. The exact result of the integral for the used speed distribution ($A = 11.1846$, $k = 2.14525$) is 8518.48 MWh. The test results are plotted in figure 14. It can be seen that the implemented quadrature rules converge to the exact integration result while Openwind

gives a worse approximation. For the default preferences in Openwind, where the integration steps are 1 m/s (24 quadrature points in this case), the computation gives an error of about 0.3 %, which is about three times the error of the trapezoidal or midpoint rule with the same step size. Gaussian quadrature is even better.

### 5.1.2 One turbine, constant power curve, wind data of one year

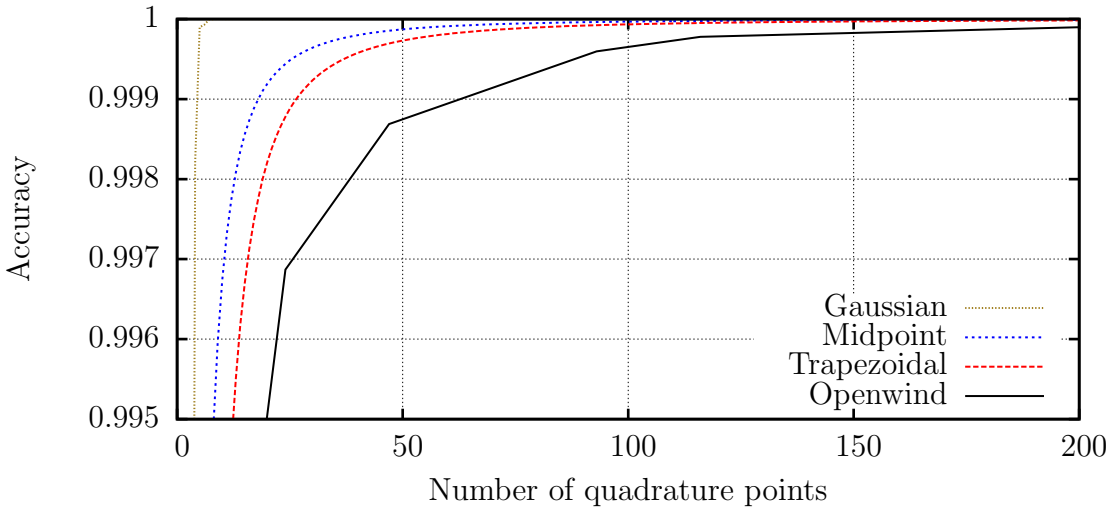


Figure 15: AEP verification: One turbine with a constant power curve

This test complies with the previous test but now it is based on measured wind data at FINO3, see section 3.2, of the year 2013. The as exact assumed reference value is the result of Gaussian quadrature with 1000 points. Figure 15 shows the results. As there is no big difference between figure 14 and 15, it can be seen that the accuracy of the quadrature methods is independent of the weighted sum over the wind directions, see equation (12).

### 5.1.3 One turbine, real power curve

In this subsection the two previous tests are repeated with a real power curve as plotted in figure 2a. The results are given in figures 16 and 17. As the accuracies for the different quadrature rules are wiggling with a changing number of quadrature points it is not possible to say, which method is the best. But it can be seen that the results of Openwind for a small range of numbers of points are similar to those obtained by the implemented quadrature methods.

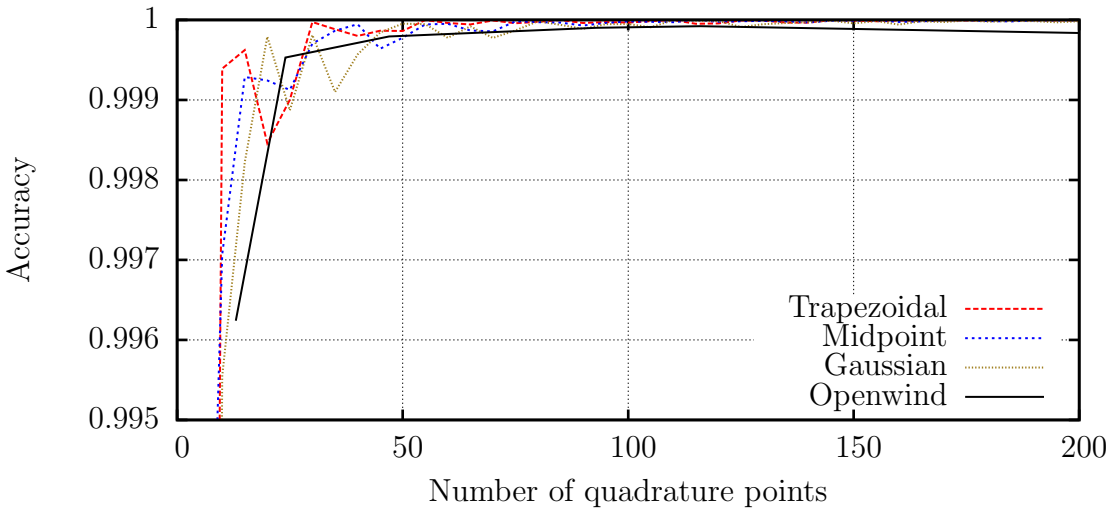


Figure 16: AEP verification: One turbine and one wind direction

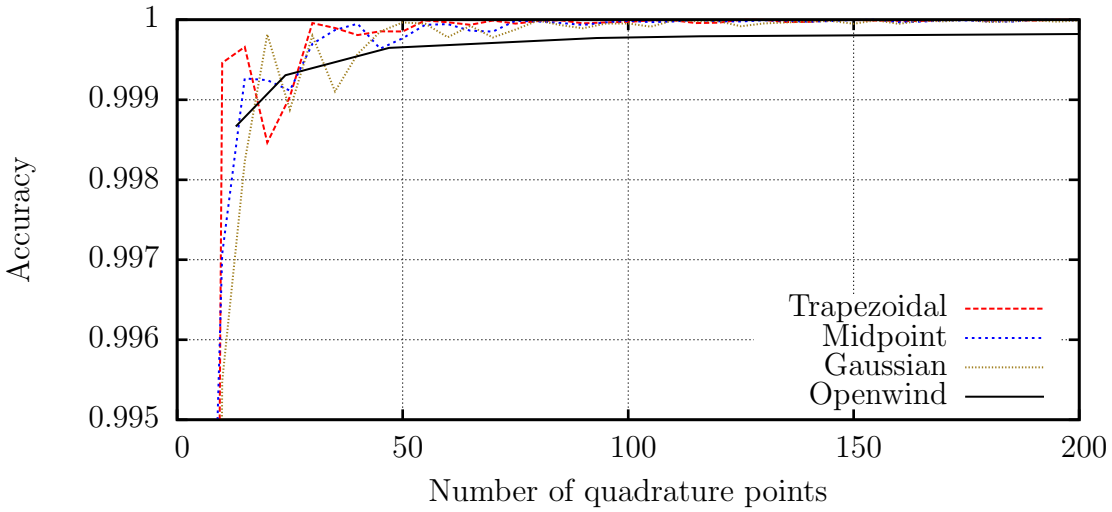


Figure 17: AEP verification: One turbine and 12 wind directions

From the above tests, where the simplest test case was checked with an analytical solution we know that we have an inexplicable discrepancy of less than 0.1 % compared to Openwind. So, for none of the following test cases our code will obtain the exactly same result as Openwind.

## 5.2 Verification of the wake models

In this section the implemented wake models are compared to Openwind and test cases from literature. The Openwind simulation parameters that are used for the wake model verification are stated in table 3. Note that only those parameters are listed, that differ from the default values.

| | |
|---|---|
| Air density lapse rate | 1E-12 kg/m$^3$/km |
| Wind speed steps | 0.1 m/s |
| Direction steps | 12 |
| Wake decay constant | 0.07 |

Table 3: Openwind simulation parameters used for wake model verification

### 5.2.1 Analytical reference value for PARK/Modified PARK

For the PARK wake model and the modified PARK model the velocity deficit and given can be calculated by hand for special cases. For this test we have two turbines in a row with a distance of $5D$, the wind comes from one direction with a constant speed. As the shaded turbine is fully inside the wake, and since there are only these two turbines, the more upwind one is standing in the free stream. The following parameters are used:

$$\begin{aligned} D &= 82\,\text{m} \\ x_{1,2} &= 5D = 410\,\text{m} \\ k &= 0.07 \\ u_0 &= 15\,\text{m/s} \end{aligned} \tag{78}$$

$C_t$ is obtained using the thrust curve of turbine type Enercon E-82. With the above assumptions equation (22) is used for the calculation of the velocity deficit at the shaded turbine and we get:

$$\delta u_{1,2} = \frac{1 - \sqrt{1 - C_t(u_0)}}{\left(1 + \frac{2kx}{D}\right)^2} = 0.0705048 \tag{79}$$

The same value can be computed when setting up this test case in the implementation.

### 5.2.2 Verification of the wake rotor intersection in the Eddy-Viscosity model

The numerical solution of the integral in equation (74) is tested by setting the initial condition as given in equation (62) to a constant value of $\frac{1}{2}u_0$. Then, two turbines

are placed, one behind the other, with a distance of exactly $2D$, so the downstream turbine is affected by the initial condition of the EV wake model. For the quadrature the number of angles $N_\varphi$ is 12 and the number of supporting points $N_r$ is chosen to be 120.

As the velocity is manually set to half the ambient velocity, the exact value of the mean velocity deficit at the downstream turbine at $x = 2D$ is 0.5. In our code the result is 0.500028, which corresponds to an error of 0.0056 %. This result is sufficiently exact.

The same test can be carried out for a Gaussian distribution instead of a constant initial condition. Here, the reference value is calculated using Mathematica[5], see appendix B. The discretization step sizes $\Delta x$ and $\Delta r$ are respectively set to $0.01D$. The wind speed is 10 m/s and the thrust coefficient $C_t$ at this speed is 0.778. In Mathematica we get a velocity deficit of 0.3708240. Our implementation yields 0.370856, i.e. the relative error is 0.0086 %.

Now we want to compare the power production of a wind turbine at 2D with Openwind. The parameters are the same as used above but now we have a wind speed distribution instead of one single speed value. The energy calculation of Openwind yields 15.6367104694 GWh, while our implementation gives 16.4306 GWh. This is an error of 6.53 %. The discrepancy leads to the assumption that the wake rotor intersection is implemented with another approach in Openwind. The same result is yielded by the following test case.

### 5.2.3 Fully shaded turbine

| | |
|---|---|
| Turbine type | Enercon E-82 |
| AEP quadrature | Trapezoidal |
| Quadrature points | 231 |

(a) General parameters

| | |
|---|---|
| Wake decay constant $k$ | 0.07 |

(b) PARK and modified PARK

| | |
|---|---|
| Turbulence intensity | 10 % |
| Discretization scheme | Crank-Nicolson |
| Solution algorithm | Thomas alg. |
| Near-wake filter | Original |
| Max. wake length | $6D$ |
| $\Delta x$ | $0.5D$ |
| $\Delta r$ | $0.2D$ |

(c) Eddy-Viscosity

Table 4: Parameters for testing wake models with two turbines in a row

The first test for checking both wake models with Openwind complies with the analytical test above (subsection 5.2.1) as the wind comes from one direction and there are two turbines standing in a row with a distance of $5D$. Now the wind speed is described by an artificial Weibull distribution (The Weibull parameters are the same as in 5.1.1). Table 4 shows the input parameters for this test scenario.

[5]Mathematica: `http://www.wolfram.com/mathematica/`

The results are stated in table 5 sorted by the wake model. For each model the result of the implementation, the result of Openwind and the relative error of the implementation, assuming Openwind is the exact result, is given.

As can be seen the discrepancy between the Eddy-Viscosity implementation and the Openwind result is very large. In the Openwind validation paper [37] their version of Eddy-Viscosity also has an even larger discrepancy to their reference. Therefore our implementation can neither proved right nor wrong using Openwind. We need to find other test cases and reference values. In the following, the models are validated separately.

### 5.2.4 Partially shaded turbine with PARK

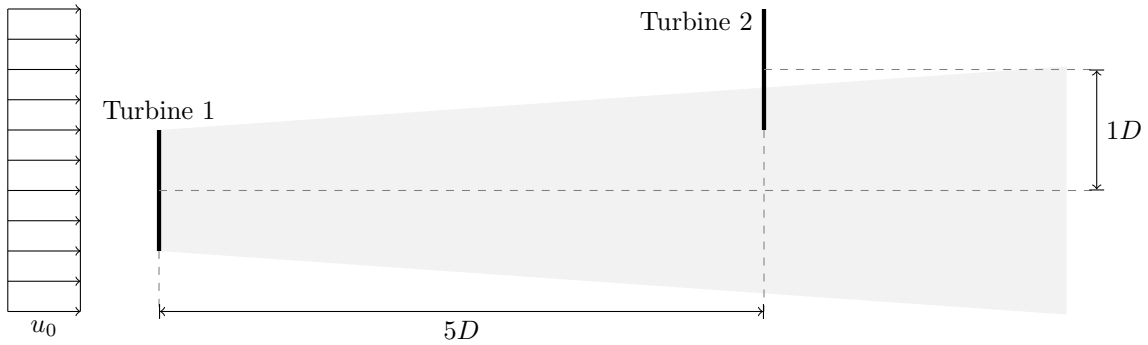


Figure 18: Test setup: Partially shaded turbine

In this test the energy output of a configuration of two turbines as shown in figure 18 is tested. The same turbine type as above is used here and the parameters given in tables 4a and 4b apply. The wind comes from one direction with the speed distribution that was already used above.

Table 6 shows the results for this test configuration. It is obvious from the last column that again a good accordance with Openwind was achieved.

### 5.2.5 Intersecting wakes

The intersecting wakes test is similar to the partially shaded turbine test but now the wake-affected turbine is affected by two intersecting wakes. The parameters for this test are the same as above and the distances between the turbines are shown in figure 19.

### 5.2.6 Ten turbines in a row

In this last test case for the PARK and modified PARK wake models there are ten turbines standing in a row on one axis with the wind direction, always with a distance of $5D$ between two turbines, see figure 20. The used wind speed distribution and

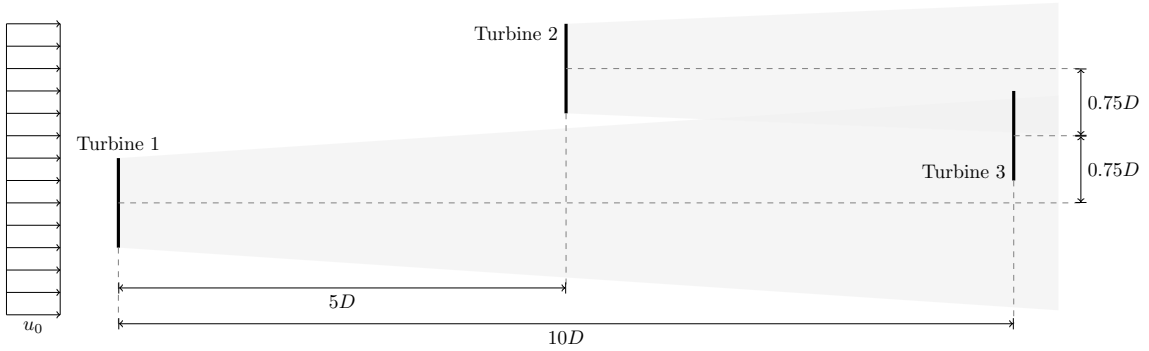


Figure 19: Test setup: Intersecting wakes

simulation parameters are again the same as in the previous tests. The results are shown in table 8.

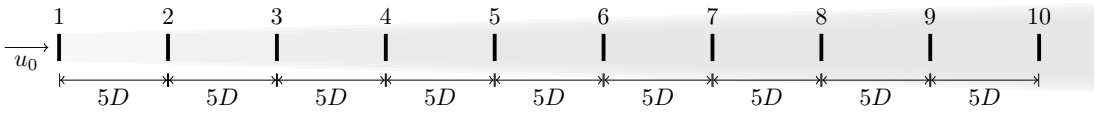


Figure 20: Test setup: Ten turbines in a row

| | **Implementation** | **Openwind** | **Error** |
|---|---|---|---|
| **No wake** | 21.0017 GWh | 20.9977 GWh | 0.019 % |
| **Original PARK** | 18.7167 GWh | 18.7154 GWh | 0.007 % |
| **Modified PARK** | 18.7167 GWh | 18.7154 GWh | 0.007 % |
| **Eddy-Viscosity** | 18.1198 GWh | 17.1532 GWh | 5.635 % |

Table 5: Test results: Two turbines in a row

| | **Implementation** | **Openwind** | **Error** |
|---|---|---|---|
| **No wake** | 21.0017 GWh | 20.9977 GWh | 0.019 % |
| **Original PARK** | 20.4429 GWh | 20.4396 GWh | 0.016 % |
| **Modified PARK** | 20.2515 GWh | 20.2484 GWh | 0.015 % |

Table 6: Test results: Partially shaded turbine

| | Implementation | Openwind | Error |
|---|---|---|---|
| **No wake** | 31.5026 GWh | 31.4965 GWh | 0.019 % |
| **Original PARK** | 30.2672 GWh | 30.2626 GWh | 0.015 % |
| **Modified PARK** | 30.1766 GWh | 30.1721 GWh | 0.015 % |

Table 7: Test results: Intersecting wakes

| | Implementation | Openwind | Error |
|---|---|---|---|
| **No wake** | 105.009 GWh | 104.989 GWh | 0.019 % |
| **Original PARK** | 77.0026 GWh | 77.013 GWh | 0.0001 % |
| **Modified PARK** | 83.6233 GWh | 83.627 GWh | 0.004 % |

Table 8: Test results: Ten turbines in a row

### 5.2.7 Development of the centerline velocity deficit

To validate the EV wake model, figure 3 from [1] is generated with our implementation of the model and compared to the original figure. The development of the centerline velocity deficit with the downstream distance is shown. For the test the ambient turbulence intensity $I_a$ is set to 14 %, the turbine hub height is 50 m and the surface roughness of the site is 0.05 m. The grid resolution is chosen as $\Delta x = \Delta r = 0.1D$.

The results of this test compared to the original results are plotted in figure 21. Unfortunately there are no exact values that can be used for comparison. Instead the results can only be compared visually with the copy of the original plot.

For further verification the EV wake computation for the simple case of one single wake was implemented in MATLAB[6], which yields the same results as the C++ implementation. The code can be found in appendix C.

The implementation of the EV wake model was not completely verified in this thesis as there are no reference results for simple test cases such as 5.2.3, 5.2.4 or 5.2.5. There are some ambiguities left in the model since the original description in the paper by Ainslie [1] is restricted to the basic idea of the model. The different implementations therefore use diverse equations for wake intersections, turbulence increase, boundary conditions, etc. and finally yield different velocity fields.

A detailed verification of the Eddy-Viscosity model in the future could consist of carefully studying the model descriptions of existing implementations, e.g. Openwind [37] or WindFarmer [13], to finally get a comparable result.

As the use of dimension in the original model description is not clear (some lengths depend on $D$), this can lead to confusion and possible errors in the implementation. It is assumed that this is the case in Openwind and thus the reason for the large discrepancy, see table 5. It is a task for the future work to prove this assumption.

[6]MATLAB: `http://www.mathworks.com/products/matlab/index.html`

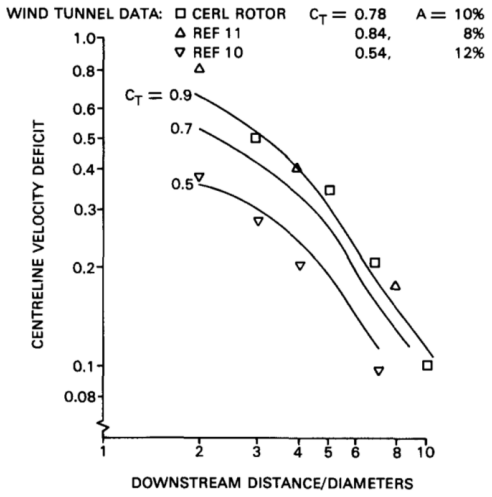


(a) Original Ainslie [1]

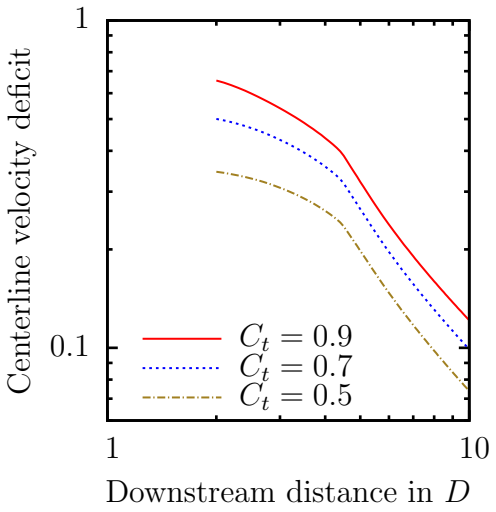


(b) Implementation

Figure 21: Development of the centerline velocity deficit with downstream distance $x$

## 5.3 Validation of discretization schemes for the Eddy-Viscosity model

In the following test the discretization grid sizes using Finite Differences and Backward Euler and Crank-Nicolson respectively are validated. Therefore, the accuracies of the centerline velocity deficit at $x = 10D$ at different values of $\Delta x$ and $\Delta r$ are plotted: Figure 22 shows the plots for the backward Euler scheme and the plot for the Crank-Nicolson method is given in figure 23. The accuracy plots vary with the thrust coefficient $C_t$ as the velocity deficit inside the wake strongly depends on this coefficient.

It can be seen that the accuracy is very sensitive to the the choice of $\Delta x$ and $\Delta r$. It is, thus, necessary to find a good choice of these parameters to achieve exact results.

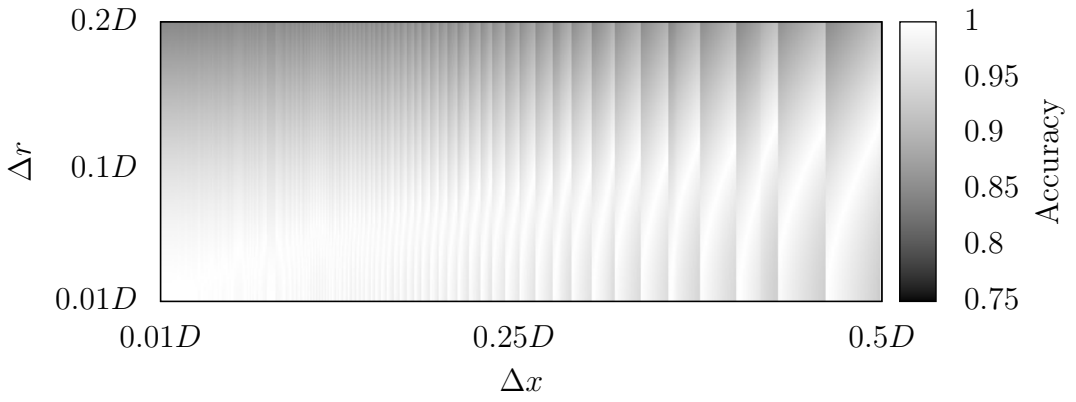


(a) $C_t = 0.086$

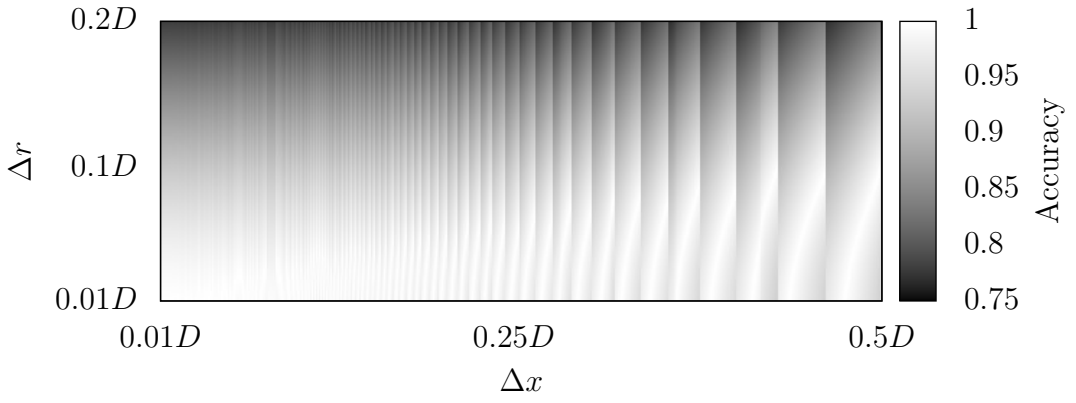


(b) $C_t = 0.778$

Figure 22: Analysis of the discretization grid size. Backward Euler

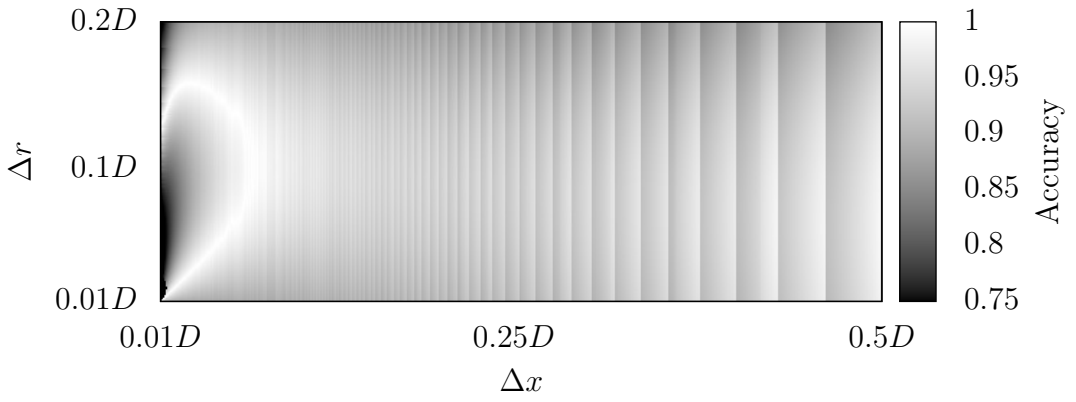


(a) $C_t = 0.086$

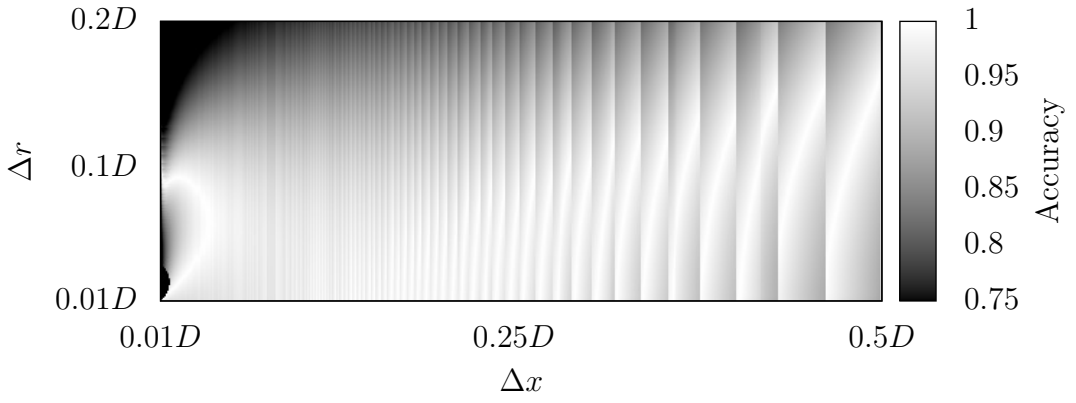


(b) $C_t = 0.778$

Figure 23: Analysis of the discretization grid size. Crank-Nicolson

## 5.4 Optimization of the Horns Rev 1 offshore wind farm

As mentioned in section 4.1 the simulation code developed during this thesis can be used as an objective function for the optimization of the turbine positions. The employed optimization method is a GA as described in [17].

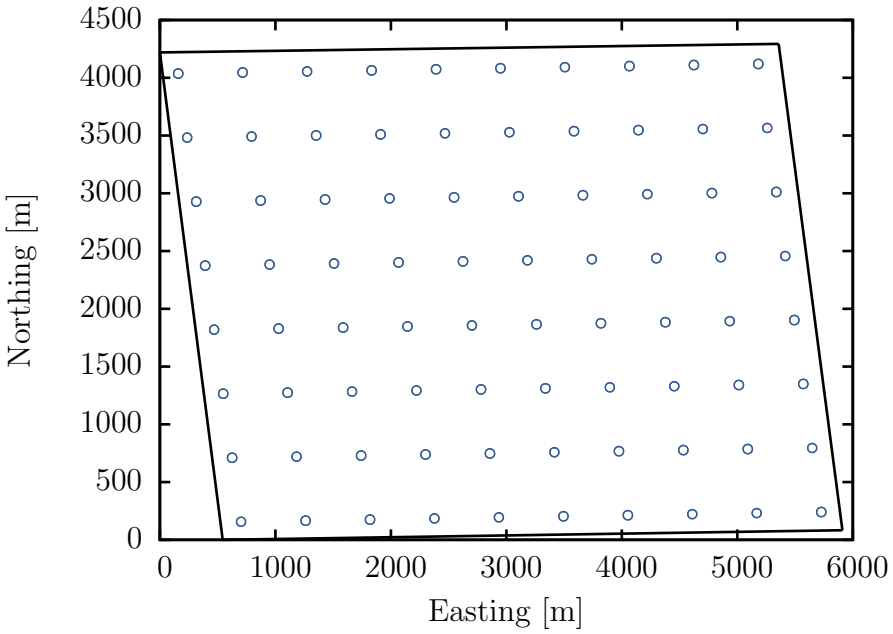


Figure 24: Layout of the Horns Rev offshore wind farm

The optimized field is the real world wind farm Horns Rev 1 in the North Sea. The wind data used to optimize the turbine field are the data measured at the FINO3 met mast from 2011 to 2014, about 50 km southwest of Horns Rev. The turbine data (power and $C_t$ curve, hub height, rotor diameter) are those provided by Jensen et al. in [18]. The positions of the turbines and the area of the site are extracted from OpenSeaMap[7].

The simulation parameters used to run the optimization are given in table 9.

| | |
|---|---|
| **Wake model** | Modified PARK |
| **Objective function** | Annual energy production |
| **Calculate wake decay constant** | False |
| **Wake decay constant** | 0.04 |

Table 9: Simulation parameters for the optimization of Horns Rev

The optimization was run twice, the first run was completely without restriction and in the second run the valid positions were given by a regular grid. When using a free optimization, the energy output was much higher than the energy output of the

[7] `http://www.openseamap.org/`

reference field (original Horns Rev layout), see figure 25. The positions after 1, 10, 50 and 100 steps are shown in figure 26.

In the restricted optimization the turbines were forced to positions on a regular grid with horizontal and vertical distances of exactly $5D$.

Figure 27 shows the AEP for the best field of each optimization step of the restricted optimization compared to the reference value, which complies with the original layout shown in figure 24.

Analogous to figure 26 in figure 28 the field layout is plotted for the first and the last step of the optimization and two intermediate steps.

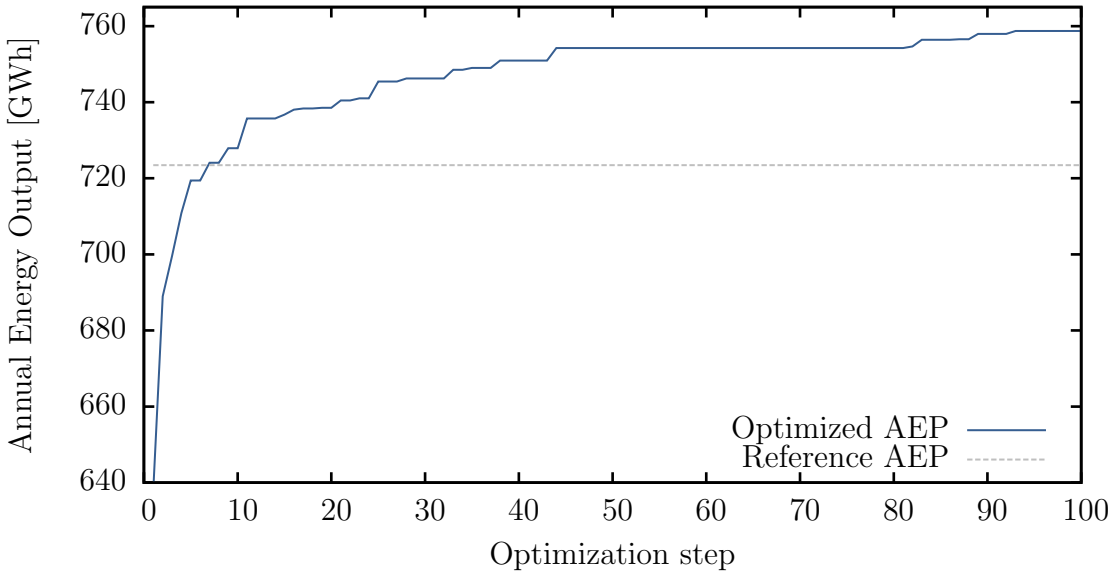


Figure 25: Convergence of a free optimization of Horns Rev

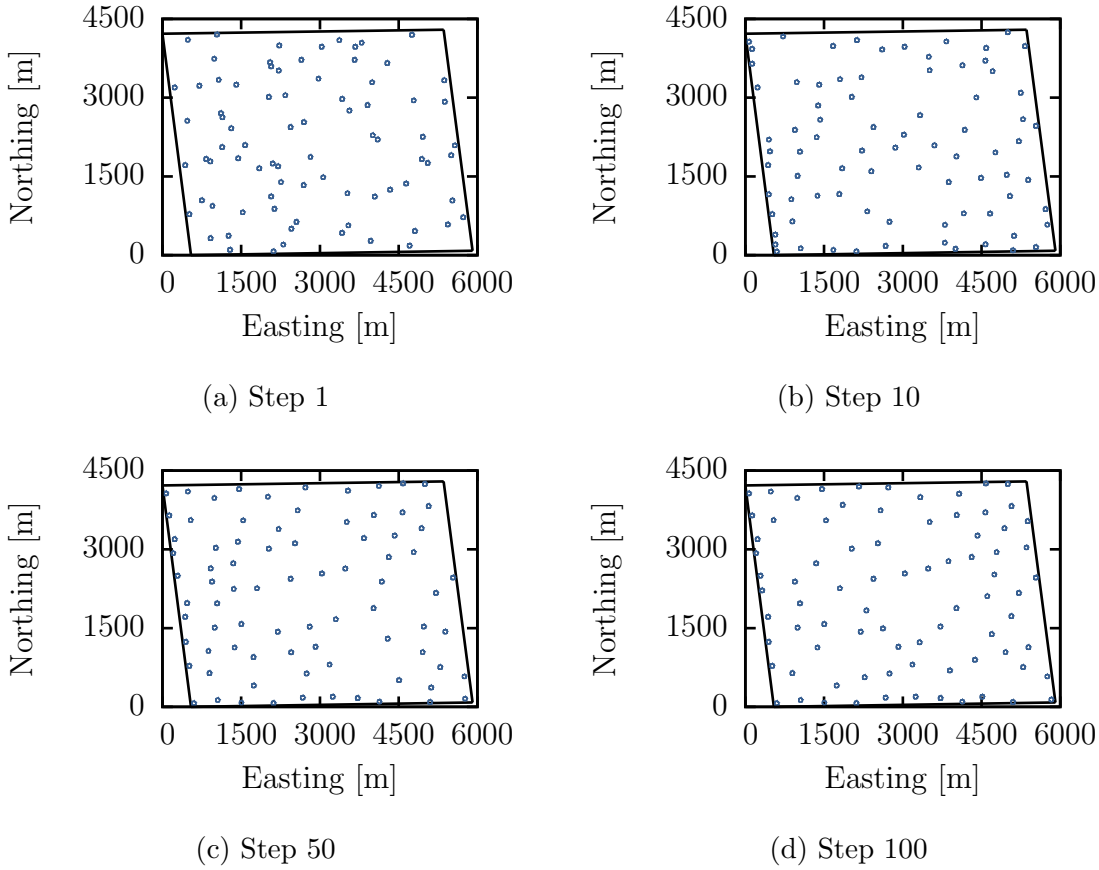


(a) Step 1

(b) Step 10

(c) Step 50

(d) Step 100

Figure 26: Freely optimized positions for the Horns Rev wind farm

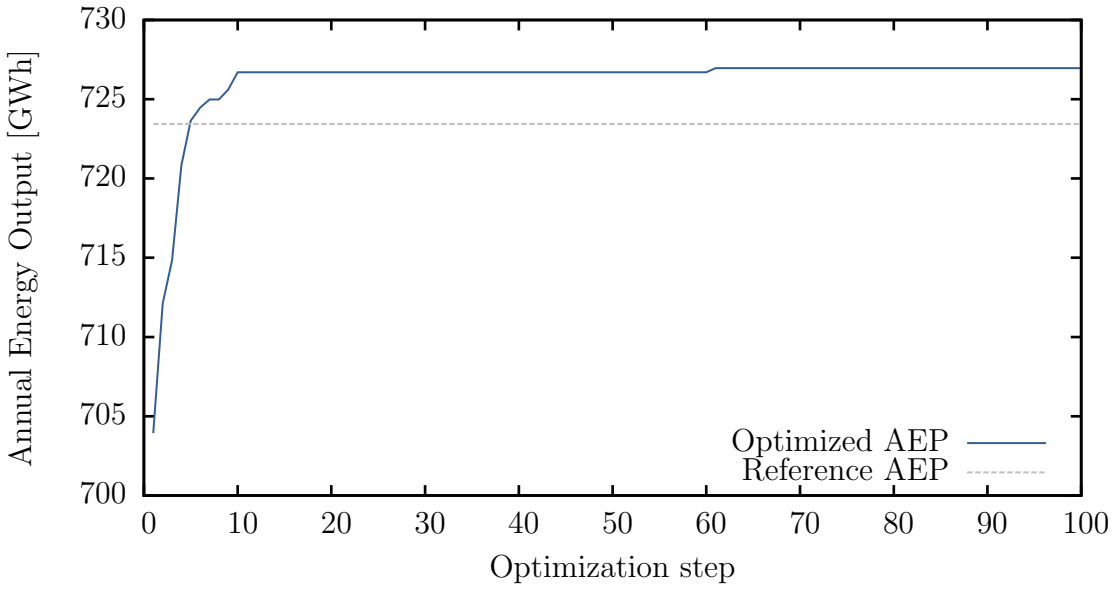


Figure 27: Convergence of the optimization of Horns Rev on a regular grid

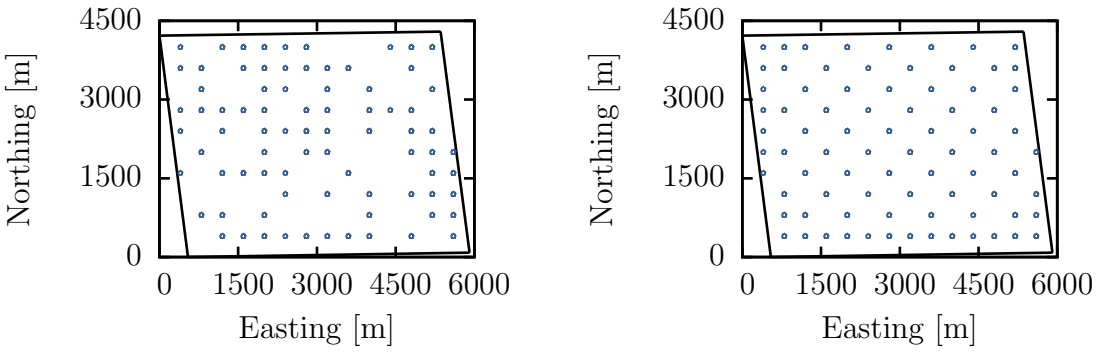


(a) Step 1




(b) Step 10

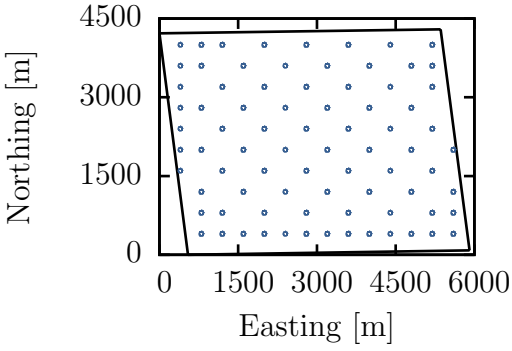


(c) Step 50

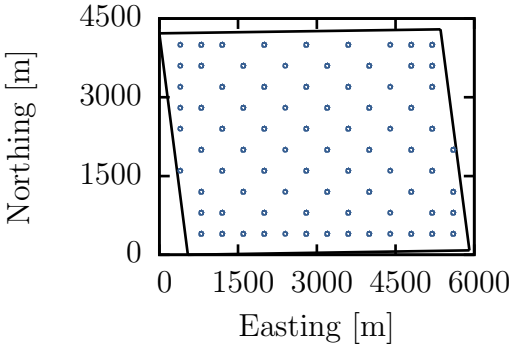


(d) Step 100

Figure 28: Optimized positions for the Horns Rev wind farm on a grid structure

# 6 Conclusion & Outlook

In this thesis the basic approach of modeling offshore wind farms was presented. There were two common wake models implemented and affiliated to an existing simulation and optimization framework. During the work on this thesis several issues and ideas came up that need to be left for the future work as they would have gone beyond the scope of this bachelor thesis. The items left for the future are listed in the following:

- As the EV wake model is not clearly defined for wake intersections and turbulence increases due to the wake, there are several variants implemented in different wind simulation programs such as Openwind and WindFarmer. An aim for the future could be to reimplement the versions of Openwind and WindFarmer and validate the code with the existing software.
- The EV model can be solved with another method than finite differences. Approaches for solving the (simplified) Navier-Stokes equations numerically can be found in literature. See for example [6] and [31].
- As the assumption of axial symmetry in the EV model strongly conflicts with reality, a generalization of the model to a non-symmetric 3D calculation should improve the accuracy of the current model.
- The physical goodness of the filter functions presented in section 3.6.1 is not yet validated. This should be done in the future.
- For the optimization it could be interesting to implement a more complex cost model and to introduce the option to optimize the number of turbines or the used turbine type.
- In the development of a new cost function the water depth could be respected: The deeper the sea, the higher the installation costs.
- The water depth could also be respected in the definition of a restricted area, e.g. turbines can only be placed where the water depth is lower than 30 m.
- Finally additional wake models could be implemented or the existing wake models could be developed further. Here, measured data are needed.

# References


[1] John F Ainslie. Calculating the flowfield in the wake of wind turbines. *Journal of Wind Engineering and Industrial Aerodynamics*, 27(1):213–224, 1988.

[2] *Openwind User Manual*. AWS Truepower, LLC, 463 New Karner Road, Albany, NY 12205 USA, July 2014. Version 1.6.

[3] RJ Barthelmie, GC Larsen, ST Frandsen, L Folkerts, K Rados, SC Pryor, B Lange, and G Schepers. Comparison of wake model simulations with offshore wind turbine wake profiles measured by sodar. *Journal of atmospheric and oceanic technology*, 23(7):888–901, 2006.

[4] Philippe Beaucage, Michael Brower, Nick Robinson, and Chuck Alonge. Overview of six commercial and research wake models for large offshore wind farms. *Proceedings of the European Wind Energy Associate (EWEA)*, 2012.

[5] M Brower and N Robinson. The openwind deep-array wake model. *Albany, NY: AWSTruePower, LLC*, 2012.

[6] Martin Burger. Numerical methods for incompressible flow. Lecture Notes, 2010. UCLA Department of Mathematics.

[7] Jungchul Choi and Martin Shan. Advancement of jensen (park) wake model. In *Proceedings of the European Wind Energy Conference and Exhibition*, pages 1–8, 2013.

[8] Technical University of Denmark (DTU) Department of Wind Energy. Wasp 11 help facility and on-line documentation. chm file, 23 October 2014.

[9] Christopher N Elkinton, James F Manwell, and Jon G McGowan. Offshore wind farm layout optimization (owflo) project: Preliminary results. *University of Massachusetts*, 2006.

[10] Yunus Eroğlu and Serap Ulusam Seçkiner. Design of wind farm layout using ant colony algorithm. *Renewable Energy*, 44:53–62, 2012.

[11] Hamid Fetouaki. Robuste schätzungen der parameter der weibull-verteilung. Diplomarbeit, Universität Kassel, January 2011.

[12] Martina Fischetti. Mixed integer programming models and algorithms for wind farm layout. Master's thesis, Università degli Studi di Padova, 2014.

[13] *GH WindFarmer Theory Manual*. Garrad Hassan and Partners Ltd, St. Vincent's Works, Silverthorne Lane, Bristol BS2 0QD England, 4.0 edition, May 2009.

[14] SA Grady, MY Hussaini, and Makola M Abdullah. Placement of wind turbines using genetic algorithms. *Renewable energy*, 30(2):259–270, 2005.

[15] Martin OL Hansen. *Aerodynamics of wind turbines*. Earthscan, 2010.

[16] Carlos M Ituarte-Villarreal and Jose F Espiritu. Optimization of wind turbine placement using a viral based optimization algorithm. *Procedia Computer Science*, 6:469–474, 2011.

[17] Georg Jennessen. Optimierung eines heliostatenfeldes unter einsatz eines genetischen algorithmus. Diploma thesis, RWTH Aachen University, March 2013.

[18] Leo E Jensen, C Mørch, PB Sørensen, and KH Svendsen. Wake measurements from the horns rev wind farm. In *European wind energy conference*, page 9, 2004.

[19] Niels Otto Jensen. *A note on wind generator interaction*. Number 2411 in Risø-M. 1983.

[20] I Katic. Program park, calculation of wind turbine park performance, release 1.3++. *Risø National Laboratory, Rosklide*, 1993.

[21] I Katic, J Højstrup, and NO Jensen. A simple model for cluster efficiency. In *European Wind Energy Association Conference and Exhibition*, pages 407–410, 1986.

[22] Matthew Lackner and Christopher Elkinton. An analytical framework for offshore wind farm layout optimization. *Wind Engineering*, 31(1):17–31, 2007.

[23] Bernhard Lange, Hans-Peter Waldl, Algert Gil Guerrero, Detlev Heinemann, and Rebecca J Barthelmie. Modelling of offshore wind turbine wakes with the wind farm program flap. *Wind Energy*, 6(1):87–104, 2003.

[24] Gunner Chr Larsen, Helge Madsen Aagaard, Ferhat Bingöl, Jakob Mann, Søren Ott, Jens N Sørensen, Valery Okulov, Niels Troldborg, Niels Morten Nielsen, Kenneth Thomsen, et al. Dynamic wake meandering modeling. Technical report, Risø National Laboratory, 2007.

[25] Xiaolan Li, Jun Wang, and Xing Zhang. Equilateral-triangle mesh for optimal micrositing of wind farms. In *Proceedings of the 14th WSEAS international conference on Computers, Corfu Island, Greece*, pages 23–25, 2010.

[26] G Mosetti, Carlo Poloni, and B Diviacco. Optimization of wind turbine positioning in large windfarms by means of a genetic algorithm. *Journal of Wind Engineering and Industrial Aerodynamics*, 51(1):105–116, 1994.

[27] Søren Ott. Fast linearized models for wind turbine wakes. In *Euromech Colloquium*, volume 508, pages 11–13, 2009.

[28] A Peña and O Rathmann. The atmospheric stability dependent infinite wind farm and wake decay coefficient. *Wind Energy, in review*, 2011.

[29] Beatriz Pérez, Roberto Mínguez, and Raúl Guanche. Offshore wind farm layout optimization using mathematical programming techniques. *Renewable Energy*, 53: 389–399, 2013.

[30] William H Press, Saul A Teukolsky, William T Vetterling, and Brian P Flannery. *Numerical Recipes: The Art of Scientific Computing*. Cambridge University Press, third edition edition, 2007.

[31] Alberto Pueyo. *An efficient Newton-Krylov method for the Euler and Navier-Stokes equations*. PhD thesis, University of Toronto, 1998.

[32] Pierre-Elouan Réthoré, Peter Fuglsang, Gunner C Larsen, Thomas Buhl, Torben J Larsen, Helge A Madsen, et al. Topfarm: Multi-fidelity optimization of offshore wind farm. In *The Twenty-first International Offshore and Polar Engineering Conference*, pages 516–524. International Society of Offshore and Polar Engineers, 2011.

[33] Lothar Sachs. *Angewandte Statistik: Anwendung statistischer Methoden*. Springer-Verlag, 2013.

[34] Michele Samorani. The wind farm layout optimization problem. In *Handbook of Wind Power Systems*, pages 21–38. Springer, 2013.

[35] Timothy Stovall, Gary Pawlas, and PJ Moriarty. Wind farm wake simulations in openfoam. *AIAA Paper*, 825:2010, 2010.

[36] Angelo Tesauro, Pierre-Elouan Réthoré, and Gunner Chr Larsen. State of the art of wind farm optimization. In *EWEA 2012-European Wind Energy Conference & Exhibition*, 2012.

[37] AWS Truepower. Openwind theoretical basis and validation. *Albany, NY, Technical Report*, 2010.

[38] LJ Vermeer, Jens Nørkær Sørensen, and A Crespo. Wind turbine wake aerodynamics. *Progress in aerospace sciences*, 39(6):467–510, 2003.

[39] PEJ Vermeulen. An experimental analysis of wind turbine wakes. In *3rd international symposium on wind energy systems*, volume 1, pages 431–450, 1980.

[40] Chunqiu Wan, Jun Wang, Geng Yang, Xiaolan Li, and Xing Zhang. Optimal micro-siting of wind turbines by genetic algorithms based on improved wind and turbine models. In *Decision and Control, 2009 held jointly with the 2009 28th Chinese Control Conference. CDC/CCC 2009. Proceedings of the 48th IEEE Conference on*, pages 5092–5096. IEEE, 2009.

[41] Chunqiu Wan, Jun Wang, Geng Yang, and Xing Zhang. Optimal micro-siting of wind farms by particle swarm optimization. In *Advances in swarm intelligence*, pages 198–205. Springer, 2010.